Gallego-Parra, S.; Vilaplana Cerda, RI.; Gomis, O.; Lora Da Silva, E.; Otero-De-La-Roza, A.; Rodríguez-Hernández, P.; Muñoz, A.... (2021). Structural, vibrational and electronic properties of alpha'-Ga2S3 under compression. Physical Chemistry Chemical Physics. 23(11):6841-6862. https://doi.org/10.1039/d0cp06417c

Structural, vibrational and electronic properties of α'-Ga_2S_3 under compression

S. Gallego-Parra[1]*, R. Vilaplana[2]*, O. Gomis[2], E. Lora da Silva[1,3], A. Otero-de-la-Roza[4], P. Rodríguez-Hernández[5], A. Muñoz[5], J. González[6], J.A. Sans[1], V.P. Cuenca-Gotor[1], J. Ibáñez[7], C. Popescu[8] and F. J. Manjón[1]

[1]*Instituto de Diseño para la Fabricación y Producción Automatizada, MALTA Consolider Team, Universitat Politècnica de València, 46022 València, Spain*

[2] *Centro de Tecnologías Físicas, MALTA Consolider Team, Universitat Politècnica de València, 46022 Valencia, Spain*

[3]*IFIMUP, Department of Physics and Astronomy, Faculty of Science, University of Porto, Portugal*

[4]*Departamento de Química Física y Analítica, MALTA Consolider Team, Facultad de Química, Universidad de Oviedo, 33006 Oviedo, Spain*

[5]*Departamento de Física, Instituto de Materiales y Nanotecnología, MALTA Consolider Team, Universidad de La Laguna, 38207 San Cristóbal de La Laguna, Spain*

[6]*Ciencias de la Tierra y Fisica de la Materia Condensada, MALTA Consolider Team, Universidad de Cantabria, 39005, Santander, Spain*

[7] *Institute of Earth Sciences Jaume Almera, MALTA Consolider Team, Consell Superior d'Investigacions Científiques (CSIC), 08028 Barcelona, Catalonia, Spain*

[8]*ALBA-CELLS, MALTA Consolider Team, 08290 Cerdanyola del Valles (Barcelona), Catalonia, Spain*

*Corresponding authors: S. Gallego-Parra (sagalpar@doctor.upv.es), R. Vilaplana (rovilap@fis.upv.es)

Abstract

We report a joint experimental and theoretical study of the low-pressure phase of α'-Ga_2S_3 under compression. Theoretical *ab initio* calculations have been compared to X-ray diffraction and Raman scattering measurements under high pressure carried out up to 17.5 and 16.1 GPa, respectively. In addition, we report Raman scattering measurements of α'-Ga_2S_3 at high temperature that have allowed us to study its anharmonic properties. To understand better the compression of this compound, we have evaluated the topological properties of the electron density, the electron localization function, and the electronic properties as a function of pressure. As a result, we shed light on the role of the Ga-S bonds, the van der Waals interactions inside the channels of the crystalline structure, and the single and double lone electron pairs of the sulphur atoms in the anisotropic compression of α'-Ga_2S_3. We found that the structural channels are responsible for the anisotropic properties of α'-Ga_2S_3 and the *A'*(6) phonon, known as the breathing mode and associated with these channels, exhibits the highest anharmonic behaviour. Finally, we report calculations of the electronic band structure of α'-Ga_2S_3 at different pressures and find a nonlinear pressure behaviour of the direct band gap and a pressure-induced direct-to-indirect band gap crossover that is similar to the behaviour previously reported in other ordered-vacancy compounds, including β-Ga_2Se_3. The importance of the single and, more specially, the double lone electron pairs of sulphur in the pressure dependence of the topmost valence band of α'-Ga_2S_3 is stressed.

Introduction

Research on Ga_2S_3 chalcogenide has increased in recent years due to its promising properties in different applications. For instance, the high specific capacity of Ga_2S_3 (theoretically estimated to be 682–1591 mAh g^{-1}) [1-4] makes it a promising anode material candidate in the field of Na-ion batteries, an alternative to the well-known commercial Li-ion batteries. In this context, recently synthesized Ga_2S_3 rods mixed with graphene have shown a reversible specific capacity of 476 mAh g^{-1} (100 cycles, current density 0.4 A g^{-1}).[5] On the other hand, many GaS_4-tetrahedron-based compounds, such as $AgGaGeS_4$,[6] $LiGaS_2$[7] and $Li_2Ga_2GeS_6$,[8] have exhibited large second-harmonic generation (SHG) efficiency and high laser-induced damage threshold (LIDT), necessary for nonlinear optical (NLO) devices. It has been demonstrated that the major contribution to the high birefringence, high SHG and high LIDT in chalcopyrites $AgGaX_2$ and $LiGaX_2$ (*X*=S, Se, Te) comes from the GaX_4 tetrahedra.[9,10] These results have motivated a systematic research on Ga_2S_3 itself[11] that has proved that both α' (monoclinic, space group (S.G.) *Cc*, No. 9, Z=4) and y (cubic "sphalerite", S.G. F-43*m*, No. 216) phases have a good optical transparency in the IR region and large NLO effects, with SHGs and LIDTs competitive with commercial NLO materials, like $KTiOPO_4$ and $AgGaS_2$. In a wider perspective of the optoelectronic industry, Ga_2S_3 is a wide-band semiconductor (2.5-3.4 eV)[12, 13] suitable for a wealth of applications, such as emitters from near IR to blue region,[14-17] UV optical absorbers,[18] Terahertz receivers,[19-21] photovoltaic devices,[22, 23] gas sensors,[24, 25] micro-tunable lasers,[26] and fluorescent probe materials.[27]

All the above applications reveal the great versatility of Ga_2S_3 and open exciting prospects for inexpensive, non-toxic, and abundant-element-based devices. Therefore, understanding the behavior of the different phases of Ga_2S_3 is necessary. According to the Ga-S phase diagram,[28, 29] the α' phase is the stable polymorph at room conditions and melts congruently at 1300 K. At high temperatures (HTs) and non-stoichiometric compositions, three phases are found: y phase between 1130-1180 K; α (hexagonal, S.G. $P6_1$, No. 161) and β (hexagonal "wurtzite", S.G. $P6_3mc$, No. 186) phases between 1190 and 1300 K depending on the excess of Ga.[30] Due to the tendency of Al, Ga and In atoms to show four-fold coordination when linked to S, Se and Te atoms, such as in zincblende-like binary *AX* compounds, like GaS, GaSe and GaTe or zincblende-related ternary ABX_2 compounds, like chalcopyrite $AgGaS_2$, $AgGaSe_2$ and $AgGaTe_2$, 1/3 of cations sites are empty in the four existing phases with Ga_2S_3 stoichiometry due to the mismatch between the number of cations and anions. The same occurs in zincblende-related defect chalcopyrite $CdGa_2S_4$, $CdGa_2Se_4$ and $CdGa_2Te_4$ and other chalcogen-based ordered-vacancy compounds (OVCs).[31-33] However, only the α' phase exhibits an ordered array of these cation vacancies. The S atoms are distributed in an almost hexagonal close-packed arrangement in α', α and β phases while they are in a cubic close-packed fashion in the y phase. In fact, α' and α phases are superstructures of the β phase, which means that Ga sites determine the resulting structure.[34] In fact, if vacancies of the α' phase were filled with cations, we would obtain a distorted wurtzite lattice;[32, 34] i.e. we would reproduce the β phase of Ga_2S_3 but without disordered vacancy arrays.

Figure 1 a) shows the monoclinic unit cell of the α' phase. This phase has 5 independent atoms, two Ga (Ga1 and Ga2) and three S (S1, S2 and S3), all occupying 4*a* Wyckoff positions. Vacancies (V) are also represented in **Fig. 1 a)**. Both Ga cations are four-fold coordinated, with Ga1 atoms linked to two S1, one S2 and one S3 atoms and Ga2 atoms linked to one S1, two S2 and one S3 atoms. In contrast, the three S atoms are coordinated differently. S1 and S2 are three-fold coordinated, S1 is linked to two Ga1 and one Ga2 atom and S2 is linked to one Ga1 and two Ga2 atoms. In turn, S3 is two-fold coordinated to one Ga1 and one Ga2 atoms. Based on the

coordination of Ga and S atoms observed in **Fig. 1 a)** and according to the Lewis diagrams (see **Fig. 1 b)**), one of the Ga-S bonds in the GaS_4 tetrahedra should be a dative bond. Furthermore, another feature (not emphasized in the literature) must be highlighted: S1 and S2 atoms have one lone electron pair (LEP), while S3 atoms have two LEPs. The greater electrostatic repulsion of these LEPs in comparison to bonded electron pairs[35] explain the decrease in symmetry and the distortion of the S arrangement with respect to the hexagonal wurtzite lattice. In particular, the LEPs give rise to empty channels lying along the *c* axis and pointing towards the ordered cation vacancies (see **Figs. 1 c)** and **d)**).[36, 37]

Several efforts have been made to explore the temperature-composition phase diagram of the Ga-S system at room pressure; however, little information is available about the Ga-S system at high pressure (HP). To our knowledge, only two studies have addressed the behaviour of Ga_2S_3 at HP.[38] Using *in situ* X-ray diffraction (XRD) and X-ray near edge structure (XANES) measurements supported by theoretical simulations, a pressure-induced phase transition from the monoclinic α' phase to the rhombohedral tetradymite-type structure (S.G. *R-3m*) was observed at 16 GPa and 1300 K.[38] Curiously, the pressure-induced stabilization of the tetradymite-like phase under pressure was also observed in other A_2X_3 compounds, as α(R)-In_2Se_3.[39] Moreover, the tetradymite-like phase is the typical phase at room conditions of heavy group-15 sesquichalcogenides (β-As_2Te_3, Sb_2Te_3, Bi_2Se_3 and Bi_2Te_3) with exceptional thermoelectric properties and is strongly related to their recently discovered topological insulating properties.[40] A most recent publication has reported Raman scattering (RS) and electrical conductivity measurements under HP, showing that the α'-Ga_2S_3 undergoes to a semiconductor-metal transformation at 11.3 (17.2) GPa under hydrostatic (non-hydrostatic) condition at room temperature.[41] Such phase at those pressures was associated to the *R*-3*m* phase, according to the previous Lai *et al.*'s results.[38] On top of that, two HP transitions have been observed under decompression, at around 8.0 and 3.0 GPa for both hydrostatic and non-hydrostatic conditions.[41] However, the lack of XRD measurements on downstroke hamper a clear identification of such polymorphs.

Cationic LEPs present on oxides and chalcogenides of groups 14 (Ge, Sn and Pb) and 15 (As, Sb and Bi) have been the subject of multiple studies under HP.[42-45] Stereochemically-active cationic LEPs (formed from the cation *s* valence electron pair) occur when the empty p orbital of the cation hybridizes with the antibonding cation *s*-anion *p* orbital. This stabilization is promoted by the small energy separation between the cationic *s* and anionic *p* orbitals.[46] This usually occurs when cations are linked to light chalcogen anions, such as O and S. For Se and Te, with a higher energy of anionic *p* orbitals, the s-p mixing is smaller and cationic inert LEPs are preferred. This seems to be the reason why the rhombohedral layered tetradymite-like structure is present in Sb_2Te_3, Bi_2Se_3 and Bi_2Te_3, as already commented. The behaviour of anionic LEPs at HP has not been studied in these layered chalcogenides and in other chalcogenides with single LEPs, like ordered vacancy compounds (OVCs).[31, 47] For example, in molecular solids like S_8 [48] and thioarsenide molecular crystals As_4S_n (n = 3, 4 and 5)[48], their HP behaviour has been studied,[49-53] but the role played by the double LEPs present in such structures under compression has not been clarified. In this context, we consider that a detailed study of the properties of α'-Ga_2S_3 under compression has not been done. More specifically, the role of the channel-like structure of the vacancies formed by the single and double LEPs of S atoms in the anisotropic compression of the α' phase has not been studied. Therefore, the presence of single and double LEPs of S atoms in α'-Ga_2S_3 makes this compound an ideal system to evaluate the influence of these two different stereochemically-active anionic LEPs on the pressure behaviour of α'-Ga_2S_3 and could shed light on the behaviour of anionic LEPs in other solids under compression.

The present work is devoted to the study of the structural, vibrational and electronic properties of the α' phase of Ga_2S_3 at HP and addresses the following points: 1) the study of the structural and vibrational properties by means of HP-XRD and HP-RS measurements, complemented with *ab initio* simulations; 2) the study of anharmonic properties arising from the joint study of the HP-RS and HT-RS measurements; 3) the characterization of the different chemical bonds and interactions and the relevance of the single and double LEPs at HP via the Quantum Theory of Atoms In Molecules (QTAIM) and electron localization function (ELF) analysis at different pressures; and finally 4) the understanding of the electronic properties under compression via *ab initio* simulations.

Experimental details

Commercial powders of α'-Ga_2S_3 were purchased from Alfa Aesar, with a high purity (99.99%). For HP measurements, powders were loaded in a 150-μm diameter hole made in an Inconel gasket and inserted in a membrane-type diamond-anvil cell with 350 μm diamond-culet diameter. A 4:1 methanol-ethanol mixture was used as a pressure-transmitting medium (PTM).[54]

Room-temperature powder angle-dispersive HP-XRD measurements up to 17.5 GPa, with cooper as a pressure sensor,[55] were carried out in the BL04-MSPD beamline at ALBA synchrotron facility.[56] The beam was focused by Kirkpartrick-Baez mirrors and images were collected using a Rayonix SX165 CCD detector, with a diameter active area of 165 mm, located at 240 mm from the sample. XRD measurements were performed with a wavelength of 0.4246 Å. The 2D x-ray diffraction area detector data and the calibration with standard LaB_6 were performed with the Python-based DIOPTAS software.[57] Le Bail method was employed in our refinements with the software GSAS-II.[58]

Unpolarized HP-RS measurements up to 16.1 GPa were carried out with a LabRAM HR UV Raman microspectrometer with a thermoelectrically cooled CCD camera and a spectral resolution better than 2 cm^{-1}. Excitation of Raman signal was performed using the He:Ne line (632.8 nm) with a power below 1 mW. The applied pressure was determined by the ruby luminescence method.[59] Raman peaks have been fitted to Voigt profiles, where the spectrometer resolution is taken as the fixed Gaussian width.

Theoretical details

Density functional theory (DFT)[60] calculations of α'-Ga_2S_3 have been carried out with the Vienna Ab-initio Simulation Package (VASP).[61] The projected augmented wave (PAW) potentials[62, 63] have been used to describe valence electrons of Ga ($4s^2 3d^{10} 4p^1$) and S ($3s^2 3p^4$) atoms, taking into account the full nodal character of the all-electron charge density in the core region but with an affordable basis-set. Calculations were performed with the generalized gradient approximation (GGA) of Perdew-Burke-Ernzenhof revised for solids (PBEsol).[64] A plane-wave kinetic-energy cutoff of 380 eV was defined in order to achieve highly converged results. For each relaxed structure, calculations were performed with the automatic k-point generation method included in the VASP package using l=30, that provides a dense special k-mesh of 6x6x5, with Hellman-Feynman forces smaller than 0.006 eV/Å per atom and deviations of the stress tensor from the diagonal hydrostatic form smaller than 0.1 GPa.

Lattice-dynamic calculations of transversal optical (TO) modes were performed at the zone center (Γ-point) of the Brillouin zone. The direct force-constant approach (or supercell method) with the primitive cell was employed for the calculation of the dynamical matrix at the Γ-point.[61, 65] In order to obtain the phonon density of states, a 4x4x4 supercell was used.

The DFT charge densities were analysed with the Critic2 program.[66] The Yu-Trinkle method,[67] implemented in Critic2, was employed to calculate Bader atomic charges and atomic volumes using VASP output files (CHGCAR and AECCAR files). In order to guarantee a smooth pressure behaviour of the topological properties at the bond critical points (BCPs), VASP-optimized structures were recalculated using the linearized augmented plane-waves (LAPW) method implemented in the Elk program, version 6.3.02.[68] For the ELK calculations, we used a 2 x 2 x 2 uniform k-point grid, R_{min} x $\max\{|\mathrm{G}+\mathrm{k}|\}$ equal to 9 and $R^{MT} = 2.4$ a.u. and 2.2 a.u. for Ga and S atoms, respectively. At each pressure, the number of critical points fulfils the Morse zero-sum condition. The kinetic, potential and total energy densities were calculated using the Thomas-Fermi approximation, with the semiclassical gradient correction proposed by Kirzhnits.[69, 70] Finally, the positions of the ELF maxima were located using Critic2 and ELF isosurfaces were obtained with VESTA software[71] by reading the cube files written by Critic2 from ELF3D.OUT files of Elk.

Structural properties under compression

Figure 2 shows selected HP-XRD patterns of the α' phase at HP up to 17.5 GPa. At 0.1 GPa, we can distinguish several diffraction peaks at angles below 12 degrees that belong only to the α' phase (at around 4.6, 5.2, 7.0, 7.6, 8.1, 8.9, 11.1 and 11.9 degrees) in good agreement with a previous HP study.[38] Above 12 degrees, our diffraction peaks from the α' phase are overlapped with those from an impurity that was also observed in a previous HP work using commercial powder.[38] Such impurity has been identified as Ga_2O_3 in the commercial sample. For further details, the authors are referred to the Supporting Information (SI) (see **Fig. S1** in the SI). To avoid misunderstanding, we include in **Fig. 2** tick marks for the phases of Ga_2S_3 and Ga_2O_3 and also Cu reflections at certain pressures. It can be observed that emerging diffraction peaks observed at HP come from the splitting of those peaks overlapped from Ga_2O_3 and the α' phase.

Le Bail refinement of the pattern at 0.1 GPa (**Fig. S1**) yields the following lattice parameters of α'-Ga_2S_3: a=11.121(6) Å, b=6.4093(3) Å, c=7.012(2) Å and β=121.276(7) degrees with a unit-cell volume of 427.16(2) $Å^3$. These values are in good agreement with those reported in earlier works.[36, 37] At HP, the shortening of the different interplanar distances in the α' phase shift the diffraction peaks at higher angles, and the same happens with the impurity and the Cu peaks. Above 3.3 GPa, several overexposed spots start to emerge in the diffraction rings, making difficult to mask such zones. That forces us to perform Le Bail refinements on regions richer in Cu, leading to a deacrease of reflection intensities of α' phase and Ga_2O_3, especially above 5.7 GPa.

At 16.1 GPa, several peak intensities of the α' phase start to decrease notably (marked with vertical arrows in **Fig. 2**). Those peaks disappear completely at 17.5 GPa, which does not allow us to refine the α' phase anymore. At this pressure, a pressure-induced phase transition is observed, in agreement with previous works.[38,41] New peaks are not observed for the HP phase, maybe due to the lack of heating to overcome a large kinetic barrier, as was suggested in **Ref. 38**. Curiously, heating has not been required for such HP transition in a recent work.[41] In any case, as previously mentioned, in this work we are only concerned with the behaviour of the α' phase at HP, so the nature and behaviour of the HP phase is out of the scope of the present paper.

As can be seen in **Fig. 3 a)**, our experimental unit-cell volumes below 2 GPa agree reasonably with those of run-2 in **Ref. 38**. At higher pressures, our experimental unit-cell volume shows a larger compression than that of **Ref. 38**. This mismatch could stem from the less hydrostatic

conditions achieved in **Ref. 38** (which used LiF as a PTM) than in this work (we have used 4:1 methanol:ethanol mixture as a PTM). We must stress that the decrease of our experimental unit-cell volume is in good agreement with the behaviour observed in both LDA and GGA-PBEsol theoretical calculations shown in **Fig. 3 a)**. Note that our GGA-PBEsol calculations show a more pronounced compression than LDA calculations up to 6 GPa,[38] and that both calculations show a similar compression rate at higher pressures.

Concerning the pressure behaviour of the α' phase, Lai *et al.*[38] employed a 2nd-order Birch-Murnaghan equation of state (BM2-EoS) to evaluate the zero-pressure volume, V_o, and bulk modulus, B_o.[38] This could be reasonable for their run-1 since fixing the pressure derivative, B_o', to 4 allowed them to fit experimental data despite not having enough points. In order to properly determine the order of the BM-EoS for our experimental data and those of run-2 of Lai *et al.* [38], we have plotted the normalised stress, F_E, vs finite strain, f_E, (**Figure S2**) by employing EosFit-7c software.[72] It can be observed that both our experimental data (**Fig. S2 a)**) and that from Lai *et al.* (**Fig. S2 b)**) fit better to a BM3-EoS than to a BM2-EoS (see **Table 1**) since B_o' values of both sets of experimental data, which are in agreement between them, are far from 4. In addition, both experimental data sets show a similar B_o and V_o.

Importantly, the experimental B_o values are between those of GGA-PBEsol (**Fig. S2 c)**) and LDA (**Fig. S2 d)**) calculations. The former is better fitted with a BM3-EoS while the latter is better fitted with a BM2-EoS. For the sake of comparison, we have also fitted the LDA data to a BM3-EoS (see **Table 1**). GGA-PBEsol data predict a softer behaviour of α'-Ga_2S_3 at HP than previously reported LDA data.[38] On the other hand, the B_o and B_o' values for α'-Ga_2S_3 are in agreement with those values previously reported for isostructural β-Ga_2Se_3 (see **Table 1**).[73, 74] Channels are expected to shrink on compression, thus leading to a low B_0 value and a values of B_0' much higher than 4, as occurs in other compounds with channels caused by LEPs.[42, 75] The obtained B_o' values for α'-Ga_2S_3 are only slightly larger than 4 for both experimental and theoretical data. A deeper study of the pressure behaviour of the LEPs forming the channels will be later provided when the evolution of the charge density at HP is analyzed.

The pressure dependence of the lattice parameters and monoclinic β angle of α'-Ga_2S_3 is shown in **Fig. 3 b)** and its inset. In general, there is a good agreement between our experimental and theoretical data on compression. We can observe that GGA-PBEsol data are closer to the experimental lattice parameters than LDA, particularly below 4 GPa. The most striking feature of the α' phase on compression is the change in behavior of the β angle at HP. The experimental (theoretical) β angle shows a negligible pressure dependence below 4 GPa (8 GPa) and a decrease above this pressure. Therefore, both experimental and theoretical data show a symmetrisation of the monoclinic structure at HP.

Regarding the axial bulk modulus of the α' phase, Lai *et al.* reported a quasi-isotropic behaviour based on the modified BM2-EoS.[38] In order to revise this assessment, we have first tabulated the zero-pressure axial compressibilities, defined as $\kappa_x = -\frac{1}{x}\frac{\partial x}{\partial P}$. As **Table 2** shows, the *b* axis is the most compressible for our experimental data and those from run-2 in **Ref. 38**. However, theoretical calculations predict the *a* axis to be the most compressible. Our experimental and theoretical data reflect a higher axial compressibility than the results from **Ref. 38**. Indeed, *a* and *b* axes are the most compressible axes of the α' phase. In view of **Table 2**, the α' phase does not have a quasi-isotropic behaviour. In any case, it must be stressed that the conclussions reached in the paragraph as a result of fitting each lattice parameter of monoclinic α'-Ga_2S_3 to a BM3-EoS or a Murnaghan-EoS cannot totally describe the change of the crystal at HP because

the β angle also changes with pressure. Consequently, a more elaborate analysis should be done of the axial bulk moduli in monoclinic and triclinic systems.

For monoclinic systems, the non-orthogonality in the three crystallographic axes implies non-zero shear stress when each axis is compressed. Therefore, a good description of the axial compressibility requires the study of the isothermal compressibility tensor. For this purpose, we have used the software PASCAL[76] with the Eulerian approximation[77] to obtain both orthogonal principal axis ev_i and their compressibilities λ_i by diagonalizing the isothermal compressibility tensor (see **Table 2**). These parameters have been tabulated in a range of pressures from 0 to 14 GPa for our experimental and theoretical data and that from Lai *et al*.[38] It can be observed that ev_2 coincides with the *b* axis and shows an intermediate compressibility. On the other hand, ev_1 and ev_3, contained in the *a*-*c* plane, are the directions of maximum and minimum compressibilities, respectively. We find that the direction of maximum compressibility (ψ_{max}, measured to the *c* axis, from *c* to *a*) for run-2 in **Ref. 38** differs almost 27 degrees from our experimental data and theoretical calculations. We must stress that the compressibilities λ_1 and λ_2 imply between the 70-80 % of the total compression. Concerning ev_3, the direction of minimum compression (ψ_{min}, measured to the *c* axis, from *c* to *a*), is quite similar in both our results and those from **Ref. 38**, with an angle between 154 and 168 degrees.

Figure 4 helps to visualize how the principal axes are related to the channels in the crystalline structure. It can be seen that ev_2 is perpendicular to the channels, along the direction connecting S1 atoms (**Fig. 4 a)**). On the other hand, ev_1 involves the small section of the channels. Specifically, the direction of ev_1 is perpendicular to the array of S2 and S3 atoms along the *c* axis (**Fig. 4 b)**). Therefore, we can say that the empty channels, concretely along their cross-sections, are responsible for most of the compression of the α' phase. The minimum direction of compression, ev_3, implies that the stiffest direction is almost perpendicular to the layers formed by coplanar GaS_4 polyhedra along the a-b plane (**Fig. 4 b)**). We can conclude, in view of the principal axes and their compressibilities, that the α' phase shows a high anisotropy due not only to its monoclinic symmetry but also to the presence of channels along the *c*-axis of the structure.

We turn now to evaluate the role of sulfur LEPs in the compression of α'-Ga_2S_3. First, we studied the change in the GaS_4 polyhedra at HP. For that purpose, the pressure dependence of the relative volume, V/V_o, of the two different GaS_4 tetrahedra was compared to that the unit-cell volume (see **Fig. S3**). A fit to a BM3-EoS yields B_o = 123.0 (99.1) GPa and $B_o^{'}$ = 3.9 (6.1) for the $Ga1S_4$ ($Ga2S_4$) tetrahedron; i.e. both tetrahedra show a different pressure behaviour despite their similar environment. Clearly, the Ga polyhedral bulk moduli are more than double than that of the unit-cell volume (see **Table 1**), thus reflecting that the major contribution to the compression of the α' structure comes from the compression of the empty channels of the structure generated by the sulfur LEPs.

To study their similarities and differences, we have analysed the influence of pressure on both GaS_4 polyhedra by examining the calculated Ga-S bond lengths, their compressbilities, effective coordination number (ECoN), distortion index, bond angle variation and quadratic elongation with the software VESTA.[71] **Figure 5 a)** and **b)** plot the change in the Ga-S bond lengths of $Ga1S_4$ and $Ga2S_4$ tetrahedra, respectively. In both tetrahedra, the three longer Ga-S bonds involve the S1 and S2 atoms (those with only one LEP), meanwhile the shortest Ga-S bond refers to the S3 atoms (with double LEPs) (**Fig. 1 b)**). Connecting with the Lewis diagram depicted in **Fig. 1 b)**, it is clear that Ga-S3 bonds can not be dative due to the double LEPs of S3 atoms. Therefore, in

each GaS_4 tetrahedron the dative bond must be associated with either the Ga-S1 or the Ga-S2 bond. The dative bond in one of these two GaS_4 tetrahedra leads to different Ga-S bond lengths in both tetrahedra, and therefore, their different pressure dependence.

Figure 5 c) and **d)** show the compressibility of each Ga-S bond for both tetrahedra when fitted to a Murnaghan-EoS. As expected, we found that the three longer Ga-S bonds in both tetrahedra are more compressible than the shortest bond. Additionally, the Ga2 tetrahedron shows two bonds with a high compressibility (above $4 \cdot 10^{-3}$ GPa^{-1}) at low pressures while the Ga1 tetrahedron shows only one bond with a high compressibility. This difference explains the softer behaviour of the Ga2 tetrahedron than the Ga1 tetrahedron at low pressure. On the other hand, the longest Ga1-S1 bond in the $Ga1S_4$ tetrahedron, named Ga1-S1*, behaves in an anomalous way: its compressibility increases slightly up to 4 GPa, and then becomes almost constant up to 16 GPa, showing the largest bond compressibility above 11 GPa. A careful examination of the structure shows that bonds Ga1-S1* and Ga2-S2* (the longest distance between Ga2-S2 atoms) are perpendicular to the layers (**Fig. 1 c)**); i.e. they are almost in the same direction of the ev_3. This result means that the direction of minimum compressibility is in fact related to how the bonds Ga1-S1* and Ga2-S2* are compressed. In fact, we could tentatively identify the Ga1-S1* and Ga2-S2* bonds as dative if we attend to the anomalous pressure dependence of their compressibilities and their relation with the direction of minimum compressibility.

The ECoN and distortion index (see **Figure S4 a)**) are equal for both GaS_4 tetrahedra at 0 GPa; however, the $Ga2S_4$ tetrahedron has a slightly higher ECoN than the $Ga1S_4$ tetrahedron at HP and, consequently, a smaller distortion index. Largest differences are observed in the bond angle variance and quadratic elongation (**Fig. S4 b)**). These parameters are larger for the $Ga1S_4$ tetrahedron over the entire pressure range. Curiously, both tetrahedra reach almost the same value of these parameters near 16 GPa, thus suggesting that Ga atoms are increasingly displaced from their centroid in both polyhedra as pressure increases and reach similar values just prior to the phase transition. The increase of both parameters is more remarkable in the $Ga2S_4$ tetrahedron, where the Ga2 atom is strongly shifted towards the S1-S2-S3 plane (inset of **Figure S4 b)**). Concretely, this increasing distortion under compression can be rooted in the different compressibilities of the Ga1-S1* and Ga2-S2* bonds, tentatively proposed as dative, compared to the other Ga-S bonds. Indeed, the increasing distortions in both polyhedra likely cause a structural instability leading to the phase transition that occurs near 16 GPa on α' phase, as we have observed (see **Fig. 2**) and was already reported in **Ref. 38** and **41.**

Finally, in order to understand the changes observed in the Ga-S bonds we have followed the relative change of the free theoretical atomic coordinates (x,y,z) of the unequivalent Ga and S atoms at HP, as can be seen in **Figs. S5, S6** and **S7** in the SI and schematized in **Figs. S8** and **S9** in the SI. Among all the features observed, included in the SI, we must stress the symmetrisation of the structure with increasing pressure, as clearly shown by the z coordinate of the Ga2 atom (see **Fig. S7 b)**). This coordinate tends to 0 close to 16 GPa thus suggesting a phase transition above that pressure, in agreement with our HP-XRD measurements and previous works.[38, 41].

To summarize the structural part, we have found a good agreement between our experimental and theoretical results in the pressure dependence of the lattice parameters and the bulk modulus. Concerning the bulk modulus, thanks to the data of **Ref. 38** and our own results, we have demonstrated a more compressible pressure behaviour of the α' phase that was previously reported and in agreement with the pressure behaviour β-Ga_2Se_3.[79] On the other hand, our results for lattice parameters match quite well with those published in **Ref. 38**; however, we have performed a detailed analysis of the pressure dependence of the axial compressibility in a

monoclinic symmetry, like that of the α' phase, by obtaining the pressure dependence of the principal axes given by the isothermal compressibility tensor. As a result, we have obtained that the compression of α'-Ga_2S_3 is rather anisotropic and that the principal axes with the maximum and intermediate compressibilities are related with the cross-sections of the channels. Moreover, the study of the Ga polyhedral volumes have revealed that the high bulk modulus of both GaS_4 tetrahedra and their low contribution to the relative volume shows the dominant role of the channels in the compression of the α' phase. Curiously, despite the high bulk moduli of both GaS_4 tetrahedra, they experiment a high distortion at HP and show a different compression due to the existence of a dative Ga-S bond in one of the two polyhedra. In particular, the bond angle variance and quadratic elongation show the largest values (almost equal for both tetrahedra) at 16 GPa. Indeed, this increase of the distortion of both GaS_4 tetrahedra and the symmetrisation of the Ga2 atoms points out to a phase transition above 16 GPa towards a more symmetric HP phase, as previously reported.[38,41]

Vibrational properties under compression and thermal expansion. Anharmonic properties.

A) Vibrational properties at HP

Now we turn to our HP- and HT-RS measurements on α'-Ga_2S_3. Group theory predicts for the non-centrosymmetric α' phase 27 IR- and Raman-active optical modes at Γ= 13 *A*' + 14 *A*'', plus three acoustic modes (2 *A*' + 1 *A*''). We have to note that all *A'* and *A''* modes are both Raman- and IR-active; therefore, can show transversal optic (TO) and longitudinal optic (LO) components; i.e. two peaks can eventually be observed for each mode. This means that up to 54 vibrational modes can be observed in the Raman and IR spectrum of α'-Ga_2S_3. In this work, experimental modes with TO and LO counterparts are indicated in the Tables and Figures; otherwise only TO counterpart is referred.

Figure 6 shows normalized HP-RS spectra up to 16.1 GPa. All the observed Raman modes have been attributed to the α' phase with no mode corresponding to the Ga_2O_3 impurity. We have observed changes in the Raman spectrum at 15.1 GPa, with broad peaks appearing at 150, 210, 410 and 460 cm^{-1}. The new broad peaks increase their intensities at higher pressures, being that located a 410 cm^{-1} the most intense. These features present at 15.1 GPa, and even more remarkable at 16.1 GPa, show the onset of the pressure-induced phase transition observed by our HP-XRD measurements and in previous works.[38,41] In fact, recent HP-RS measurement locate the onset of the phase transition at 11.3 and 17.2 GPa under hydrostatic (helium as PTM) and non-hydrostatic (no PTM) conditions, respectively.[41] Therefore, the slight differences in this transition pressure could come from the different hydrosticity conditions achieved in both the present work and the previous ones.[38, 41] The RS spectra of **Figure 6** are in agreement with those published recently in **Ref. 41**, only differing in the transition pressure, as already commented, and the lack of measurements below 100 cm^{-1} in **Ref. 41**. Unfortunately, we can merely make a visual comparison between our HP-RS measurements and those from **Ref. 41** due to the lack of assignment of the symmetry and pressure coefficients of the observed Raman modes.

The RS spectrum of the α' phase can be divided into two regions: the low-frequency region (below 200 cm^{-1}) and the high-frequency region (above 200 cm^{-1}). According to Lucazeau *et al.*, modes at the low (high)-frequency regions correspond to bending (stretching) vibrations of the GaS_4 tetrahedra.[78] We have observed and followed the pressure dependence of 26 Raman-active modes. As observed in previous studies,[20, 22, 25, 26, 78-82] the RS spectrum at 0.5 GPa is dominated by the breathing mode near 230 cm^{-1}, which is assigned to the *A*' symmetry. This

peak is related with the symmetric stretching vibration of S atoms around the vacancies in the S atom-vacancy direction, and it derives from the symmetric Ga-S stretching vibrations of GaS_4 units.[20, 26, 78, 79] It is worth mentioning that the breathing mode is also found in adamantine OVCs of AGa_2S_4 stoichiometry,[31, 83, 84] which are synthesized from Ga_2S_3 and several binary *A*S (*A*= Zn, Cd and Hg) compounds. Their crystalline structures are strongly dominated by the Ga_2S_3 compound and have ordered vacancies, therefore explaining the presence of the breathing mode.[80-82] Moreover, the symmetric stretching mode of S anions around Ga cations has been also observed in GaS near 190 cm^{-1};[85] i.e. at a smaller frequency than the breathing mode in Ga_2S_3, likely due to the influence of the Ga-Ga bond in the vibration of the Ga_2S_6 units in GaS. Finally, we can mention that RS spectra with similarities to that of Ga_2S_3 have also been recently reported for the mc64 and mC16 polymorphs of $CsGaS_2$, constituted by corner-sharing and edge-sharing GaS_4 units, respectively, and showing no cation vacancies in their structures.[86]

To better understand the vibrational modes attributed in **Figure 6**, we have plotted the atomic displacements of some of the more representative Raman-active modes of α'-Ga_2S_3 in **Figs. S10** to **S19** in the SI. In short, we have observed that modes below 200 cm^{-1} are mainly a mixture of Ga-S bending modes and external modes of the GaS_4 units due to translation and rotation of the tetrahedra (see **Figs. S10** to **S14**). Between 200 and 300 cm^{-1}, modes are mainly Ga-S bending modes with some admixture of Ga-S stretching modes. In particular, the strongest Raman mode is the breathing mode near 230 cm^{-1} and corresponds to the *A'*(6) mode; a mixture of Ga-S bending modes leaded by displacements of S1, S2 and S3 atoms (see **Fig. S15**). The concerted displacements of S atoms lead to a strong symmetric Ga-S stretching mode of S atoms vibrating around the vacancy and to a small symmetric Ga-S stretching ν_1 mode of the GaS_4 units.[77] This is the reason why this mode is also known as the breathing mode of the vacancy. Finally, modes above 300 cm^{-1} are mainly asymmetric Ga-S stretching modes (deriving from the ν_3 mode of GaS_4 units)[77] with some admixture of Ga-S bending modes (see **Figs. S16** to **S19**).

We now turn to analyze the contribution of the different atoms to each vibrational region. For that reason, we have studied the one-phonon density of states (1-PDOS) at 0 GPa (see **Fig. S20**). Notably, our 1-PDOS is similar to that found in the Materials Project Database.[87] The 1-PDOS shows that the high-frequency region (above 200 cm^{-1}) can be subdivided into three parts: low (200-300 cm^{-1}), medium (300-350 cm^{-1}), and high (above 350 cm^{-1}). The contributions of Ga and S atoms are rather similar in the low-frequency region (below 200 cm^{-1}) and in the low part of the high-frequency region (200-300 cm^{-1}). However, in the medium and high parts of the high-frequency region there is a much larger contribution of S atoms than of Ga atoms. Concretly, S1 and S2 atoms (both with three-fold coordination) are predominant in the medium frequency region, meanwhile the S3 atoms (with two-fold coordination) contribute mainly in the high part of the high-frequency region. On the other hand, it is remarkable that the S3 atoms vibrate with low amplitudes when S1 and S2 atoms vibrate with higher amplitudes and conversely. This can be understood as a way to minimize the electrostatic repulsion between the double LEPs from S3 atoms and the single LEPs of S1 and S2 atoms.

The same three phononic gaps observed on the 1-PDOS of α'-Ga_2S_3 are seen in β-Ga_2Se_3, whose 1-PDOS can be found in the Materials Projects database.[87] A further comparision can be made if we take into account other OVCs of AGa_2S_4 stoichiometry (*A* = Zn, Cd and Hg) with tetragonal defect chalcopyrite structure (S.G. $I\bar{4}$, No. 82, Z=2),[87] which exhibit only two phononic gaps. On the other hand, the wurtzite type-structure such as ZnS, with no vacancies, only exhibits one phononic gap in its 1-PDOS.[87, 88] In this context, we can assume that the presence of vacancies in a compound gives rise to more inequivalent atoms in the asymmetric unit cell (five for α'-

Ga_2S_3, four for AGa_2S_4 and two for wurtzite type-structure). Curiously, the more inequivalent atoms, the more phononic gaps can occur in the 1-PDOS. The same trend cannot be observed in OVCs with AGa_2Se_4 stoichiometry,[87] that even do not have a single phononic gap. The reason is the overlapping of the different regions due to the reduced range of frequencies where all phonons occur as a consequence of the higher mass of Se than S. Therefore, the appearance of these phononic gaps seems to clearly depend on the mass of the atoms.

Figure 7 shows the pressure dependence of the experimental and theoretical Raman-active mode frequencies of the α' phase. Note that theoretical mode frequencies refer only to the TO counterpart. In order to do the tentative assignment of the experimental Raman-active modes shown both in **Fig. 7** and **Table S1**, we have compared our experimental frequencies and pressure coefficients with those for the TO components of the theoretical vibrational modes and also with the frequencies at room pressure reported in previous works. As observed, the rather good agreement of experimental and theoretical frequencies and pressure coefficients has allowed us to tentatively assign the symmetry of each experimental mode observed in the α' phase (see **Table S1**). It must be recalled that all *A'* and *A''* modes can show a TO-LO splitting, so two modes can be expected for each theoretically predicted mode in both RS and IR spectra. Therefore, the relatively similar frequencies shown for several *A'* and *A''* modes, coming from Raman- and IR-active modes if symmetry would be higher,[78] could be the TO and LO component of a single mode. In this respect, we have tentatively assigned the LO counterparts of some phonons to modes whose pressure coefficients do not match well with theoretical TO modes of similar frequencies.

As regards the pressure coefficients, we have found that the *A'*(6) mode has the highest pressure coefficient (~8.0 cm^{-1}/GPa) of all vibrational modes, as occurs for the breathing mode of isostructural β-Ga_2Se_3 (at 155 cm^{-1})[72] and for the breathing mode (A^1 mode) of defect chalcopyrites as $ZnGa_2S_4$, $CdGa_2S_4$ and $HgGa_2S_4$.[31, 83, 84] In the low-frequency region, most modes of α'-Ga_2S_3 show a very small pressure coefficient. Moreover, the *A'*(1) and *A''*(1) modes; i.e. those with the lowest frequency, exhibit negative pressure coefficients. This has also been observed in a number of compounds, including adamantine-type AB_2X_4 OVCs.[31, 47, 83, 84] The anomalous decrease of the frequency with increasing pressure of many Raman-active low-frequency modes cannot be explained by an increase of the cation-anion distances with increasing pressure in all these compounds. Instead, it is likely related to an instability of those structures to hydrostatic compression that is evidenced by negative pressure coefficients of low-frequency vibrational modes at the Brillouin zone edge of the cubic lattice (mainly coming from acoustic branches folded into the zone center of low-symmetry structures).[89] In the low-frequency region, the overlapped Raman peaks are easily discerned thanks to their intensities. According to the idealised P.G. proposed by Lucazeau for the α' phase,[78] the *A'* modes derive from Raman-active modes and the *A''* modes from IR-active, therefore giving arise a higher intensity for the former than for the latter. As an exception, the *A''*(3) mode is identified as more intense than the *A'*(3) mode and both modes have been confirmed by the agreement between their experimental and theoretical pressure coefficients (see **Table S1**). In terms of pressure coefficients, the mode at the right side of the A'_{TO}(5) mode does not match well with the theoretically predicted for the *A''*(4) mode; therefore it has been labelled as A'_{LO}(5). On the other hand, the high-frequency region shows a massive overlapping of the Raman peaks, and their low intensity hampers their uncoupling even at high pressure except for the *A'*(12) mode that was also previously observed.[20, 25, 78, 90] In this region, we consider that the theoretically predicted *A''*(7), *A''*(9), *A''*(10), *A''*(12), *A''*(14) modes have not been experimentally observed either in this

work or in previous ones. Instead, we have tentatively assigned the LO counterparts of the *A'*(8), *A''*(11), *A'*(11) and *A'*(13) modes in view of the mismatch between their pressure coefficients with those theoretically predicted and the higher frequencies observed. The modes of the high-frequency region exhibit higher pressure coefficients than in the low-frequency region (see **Table S1**). It must be noticed that the theoretical mode frequencies in the high-frequency range underestimate those observed experimentally, mainly above 325 cm^{-1} from the *A''*(11) to the A'_{LO}(13) modes (**Figure 7**). Moreover, it can be noticed that, in general, the modes at the lower part of the high-frequency region show larger pressure coefficients than those at the high part of the high-frequency region and are more separated at 0 (162 cm^{-1}) than at 12 GPa (135 cm^{-1}). These features of these modes, related to TO and LO modes from the cubic structure, respectively, indicate a decrease of the LO-TO splitting on increasing pressure as expected from the more covalent character of the compound on increasing pressure as is also observed in adamantine-type AB_2X_4 OVCs.[31, 47, 83, 84]

In order to evaluate the anharmonicity of each vibrational mode, we have calculated the isothermal mode Grüneisen parameter, γ_i^T (**Eq. 1** in the SI). In general, we observe a good agreement between theoretical and experimental γ_i^T. Excluding the *A'*(1) and *A''*(1) modes, which exhibit negative γ_i^T, most modes show positive γ_i^T values between 0 and 1. The only exception is the breathing mode *A'*(6) that features the highest γ_i^T with a value above 1. This result highlights the high anharmonicity of the stretching vibration of S atoms around the cation vacancies. Taking into account the microscopic definition (**Eq. 3** in the SI), the isothermal averaged Grüneisen parameter, γ_{av}^T, obtained for the α' phase from our experimental and theoretical data are 0.49 and 0.44, respectively. These values are in a good agreement with the common range for γ_{av}^T in tetrahedral compounds (between 0.5 and 1.5).[91]

B) Vibrational properties at HT

Figure 8 shows the normalized Raman spectra in the α' phase at room pressure and at selected temperatures. To assign the corresponding symmetry to each mode observed at HT, we have used the mode frequencies calculated at 0 GPa. However, due to the lack of lattice-dynamical calculations at HT, we were not able to decouple *A''*(3) and *A'*(3) modes. For that reason, we have noted them as the *A''*(3)/*A'*(3) mode. From 300 to 923 K, all observed modes shift to lower frequencies, even the the *A'*(1) and *A''*(1) modes that show softening at HP. At 948 K, the mode intensities decrease significantly and only the *A''*(3)/*A'*(3), *A'*(4), *A'*(5), *A'*(6), *A'*(12) modes from the α' phase can be discerned. However, new peaks arise at 160, 200, 320 and 410 cm^{-1} at this temperature. At temperatures above 1000 K, all modes of the α'-phase disappear but the new modes persist (see **Fig. S21**). The disappearance of the Raman-active modes of the α' phase is consistent with its melting point at about 1300 K.[28, 29] Therefore, we attribute the new Raman peaks above 948 K to the impurity of Ga_2O_3 present in the sample (see discussion in the SI in relation to **Fig. S21**).

Figure S22 shows the temperature dependence of the observed mode frequencies in α'-Ga_2S_3 and temperature coefficients are summarized in **Table S2**. The mode frequencies show a normal shift to lower frequencies as temperature increases, even the *A'*(1), *A'*(7), *A''*(8), *A'*(9) and A''_{LO}(11) modes. However, these modes exhibit a positive linear temperature coefficient but a negative nonlinear coefficient, dominating their temperature dependence behaviour.

Moreover, we can observe that the modes from the high-frequency region are more sensitive to temperature than those in the low-frequency region.

According to the Klemens model (**Eq. 5** in the SI), we have obtained the cubic and quartic anharmonic contributions, i.e. A and B coefficients, and their absolute ratio |A/B| for all the experimentally observed modes under HT. As can be observed in **Table S2**, low-frequency modes show |A/B| values above 1; i.e. with cubic anharmonic contributions dominating over quartic contributions. On the contrary, the |A/B| ratio is lower than 1 in the high-frequency region, leading to a major contribution of quartic anharmonic contributions.[92] Therefore, we can confirm that high-frequency modes have an important nonlinear temperature dependence (higher b_2 coefficients), where fourth-order processes are quite relevant. As an exception, the low-frequency *A'*(1) and *A''*(5) modes have a similar |A/B| ratio as the high-frequency modes, thus indicating a relevant contribution of fourth-order processes in these modes. In contrast, the high-frequency *A'*(8) and *A'*(10) modes have a similar |A/B| ratio as the low-frequency modes, with a clear third-order processes dominance. Concerning the *A'*(6) mode, it shows the highest |A/B| ratio so it has the highest contribution of third-order processes.

Since the *A'*(6) mode is not overlapped with other modes, we have analysed its linewidth (full width at half maximum, FWHM) under HT (**Eq. 6** from SI). The fit of FWHM data of the *A'*(6) mode at HT to **Eq. 6** in the SI yields Γ_o= 4.15 cm^{-1}, C= 0.002 cm^{-1} and D= 5.62·10^{-7} cm^{-1}, where C and D are the cubic and quartic anharmonic contributions, respectively. These values again indicate a dominance of third-order processes in the phonon-phonon coupling of the breathing mode at low temperatures. However, fourth-order processes become dominant in the FWHM shift above 300 K (see **Fig. S23**).

On the other hand, we have calculated the isobaric and isochoric mode Grüneisen parameters, γ_i^P and γ_i^V, in order to estimate the implicit and explicit effects that govern the frequency shifts observed at HT (**Eq. 7** and **8** in the SI). **Table S2** summarizes γ_i^P, γ_i^T and γ_i^V for each experimental Raman-active mode at room temperature. If the quasiharmonic approximation is valid, each γ_i^V must be equal to 0, which means a negligible explicit effect. In fact, we observe that γ_i^V values are quite similar to those of γ_i^P for the α' phase, so that there is a high contribution of the phonon-phonon coupling to the total thermal frequency shift.

In order to visualize the contribution of the implicit and explicit effects for each mode,[93, 94] we have plotted in **Figure 9** the isobaric temperature derivative (the total thermal effect, the left-hand side of the **Eq. 7** in the SI) vs the isothermal pressure derivative (the implicit effect, the first term in the right-hand side of the **Eq. 7** in the SI). The dashed lines are labelled with its corresponding implicit fraction, η_i (**Eq. 9** in the SI), which specifies the ratio of the implicit and total effects. For η_i = 0 (γ_i^T= 0) there is only contribution of the explicit effect to the mode frequency shift at HT. On the other hand, for η_i = 1 (γ_i^V= 0) the implicit effect is responsible for the mode frequency shift at HT. Finally, for η_i = 0.5 (γ_i^T= γ_i^V), both effects are comparable and for values η_i > 1 (γ_i^V< 0) both effects have opposite signs. Notice that negative η_i is similar to η_i > 1, but only changing which effect is negative (γ_i^T < 0). **Table S2** shows η_i for each mode observed. In view of **Figure 9**, we can see that most modes have η_i < 0.5, implying a predominantly explicit effect. The modes of the low-frequency region (0.01 < η_i < 0.09) exhibit a higher explicit effect than those of the high-frequency region (0.07 < η_i < 0.30). A high contribution of the explicit effect has also been observed in several transition metal dichalcogenides.[94, 95] Concerning the lowest frequency modes, the *A'*(1) and *A''*(1) modes have

negative η_i, the latter with a higher explicit effect than the former. These negative η_i stem from their softening behaviour under HP, as has been observed for many modes on As_2S_3, β-$GeSe_2$, $SnGeS_3$ and SnSe.[43, 96-98] On the other hand, the *A'*(9) and *A''*(8) modes from the high-frequency region show $\eta_i > 1$, with a highly relevant implicit effect, but small explicit effect of the opposite sign. For the *A'*(6) mode (the breathing mode), the explicit contribution is almost three times higher than the implicit one ($\eta_i \approx 0.25$).

In summary, we have studied the pressure and temperature dependence of the Raman-active modes of the α' phase, evidencing the onset of the pressure-induced phase transition at 15.1 GPa and its thermal stability until reaching the melting point at about 1300 K. Moreover, the combination of the experimental measurements and theoretical calculations has allowed us to assign tentatively the symmetries of the experimentally observed Raman-active modes. On the other hand, our calculations have lead us to highlight the mixed bending-stretching character of the Raman-active modes, with a remarkable vibration amplitude of Ga and S1 and S2 (S3) atoms in the low-frequency region and lower (high) part of the high-frequency region, respectively. Finally, the combination of HP-RS and HT-RS measurements has enabled us to address the anharmonic effects, yielding a relevant contribution of third (fourth)-order processes in the low (high)-frequency region and a high dominance of the implicit effect in most modes. Particularly, the breathing mode features the highest anharmonicity at HP (γ_i^T) and the highest contribution to the third-order processes to its frequency and FWHM at HT.

Topological analysis of the electron density under compression

Bader's quantum theory of atoms in molecules (QTAIM)[99] is based on a partition of any electronic system in real space into non-overlapping basins, whose interatomic surfaces satisfy the zero-flux condition. Critical points (CPs) are those points where $\nabla\rho(r)$ vanishes. For the chemical point of view, the bond critical points (BCPs) are CPs linking every pair of atoms along a unique path, the bond path. The nature and strength of these interatomic bonds can be evaluated using the properties at the BCPs. The basin partition also allows the integration of atomic properties, like atomic volumes and atomic charges. Concerning the α' phase, **Figure S24 a), b)** and **c)** show the evolution of atomic volumes, Bader atomic charges (Q_i) and charge transfers (CT_i) for S and Ga atoms under compression, respectively. Due to the more diffuse distribution of $\rho(r)$ in anions than cations,[100] the S basins have larger volume than Ga basins, around twice at 0 GPa (see **Figure S24 a)**). Furthermore, S3 atoms (with double LEPs) have a larger atomic volume in comparison to S1 and S2 atoms (with single LEPs). Since all basin properties are additive and these basins fill the space to give the total unit-cell volume, macroscopic properties, such as the bulk modulus, can be obtained by the volume-weighted sum of the contributions in each basin (**Eq. 10** in the SI).

According to this fraction, the S atoms represent 75% of the unit-cell volume and, therefore, their contribution dominates the crystal compressibility, in the same way as oxygen and halogen anions dominate in oxide spinels and alkali halides.[101] By fitting each $V_i(P)$ to a BM3-EoS (not shown), we have obtained for S1(2), S3, Ga1, and Ga2 basins a bulk modulus of 38.5, 31.9, 80.0, and 66.4 GPa, respectively. In this way, a global bulk modulus of 45.0 GPa is obtained for the α' phase in reasonable agreement with experimental and theoretical values (see **Table 1**). The above results show that the Ga basins are less compressible than the S basins. This is consistent with the high bulk modulus of both GaS_4 tetrahedra as compared to the total volume bulk modulus, as previously discussed. On the other hand, the smaller bulk modulus of S3 atoms compared to S1(2) atoms is explained by the greater compressibility of the double LEPs than the single LEPs. This point reinforces our previous statement that the compressibility of the α' phase

is dominated by the channels, whose behaviour under compression is determined by single and double LEPs inside the channels.

The Bader charges of the different basins, Q_i, under compression (see **Figure S24 b)**) are far from their nominal oxidation states (OS_i). These deviations increase under increasing pressure, thus pointing to a decrease of the ionicity of the compound at HP. It is worth noting the difference in terms of atomic charge between S1(2) and S3 atoms, probably due to the different number of LEPs. In order to emphasize the change in ionicity, we have plotted the charge transfer (**Figure S24 c)**), using the **Eq. 11** in the SI. The CT of Ga1, Ga2 and S1 basins decrease almost linearly. For the S2 basins, the CT flattens above 8 GPa, and for the S3 basins it decays nonlinearly. Again, the presence of the double LEPs on the S3 atoms is seen, not only in terms of CT, but also in the pressure dependence of this dimensionless parameter. Moreover, the fact that S2 atoms face the S3 atoms along the channels could explain the CT flattening of the S2 basins above 8 GPa. To get a global idea of the ionicity of the whole unit cell, we can average the CT for all the basins.[102] As a result, we have tabulated an average CT of 39.2 and 38.5 at 0 and 16 GPa, respectively. Both averaged CTs fall in the range of polar compounds (30-60), including most III-V crystals and nitrides,[102] and suggests a slight decrease in the ionicity of α'-Ga_2S_3 at HP.

To obtain relevant information about the chemical bonds present in the α' phase, we now turn to inspect the topological properties of the BCPs (**Figure S25**). While Ga-S BCPs are located along Ga-S bonds, S-S BCPs fill the channels, except for the S3-S3 BCPs. The appearance of the S-S BCPs occurs because anionic basins share their surfaces not only with cation basins, but with nearest anionic basins as well. In this sense, the S-S BCPs found are associated to the shared IASs among the S basins. Most of the S-S BCPs involve contacts between S3 atoms with other S3 atoms and with S1 and S2 atoms. The BCPs related to the S3 atoms indicate a distorted form of the S3 basins, which is likely associated with the double LEPs present inside the S3 basins.

Figure 10 a) and **b)** show the pressure dependence of $\rho(r)$ and its Laplacian, $\nabla^2\rho(r)$, for every BCP, hereafter named ρ_b and $\nabla^2\rho_b$. We can distinguish the chemical interactions into two great realms depending on the sign of the Laplacian:[99] $\nabla^2\rho_b < 0$ for shared-shell (SS) interactions (covalent and polar bonds) and $\nabla^2\rho_b > 0$ for closed-shell (CS) interactions (ionic bonds, H-bonds and van der Waals (vdW) interactions). According to these criteria, all BCPs of α'-Ga_2S_3 are found to exhibit CS interactions. In particular, Ga-S interactions are categorized with ionic bonding due to the high ρ_b and $\nabla^2\rho_b$ of Ga-S BCPs. Conversely, S-S interactions are typical vdW interactions due to their low values of these topological properties in S-S BCPs. Due to the non-directionality of the vdW interactions, these S-S BCPs at certain positions in the crystal inform about vdW interactions inside the channels. For every BCP, the ρ_b and its $\nabla^2\rho_b$ increase at HP, as expected. However, the $\nabla^2\rho_b$ for the Ga2-S3 BCP increases smoothly until it decreases slightly above 14 GPa. We discuss this result below. For S-S BCPs, this increase indicates the increase of the vdW interactions inside the channels. Among these BCPs, S3-S3 BCPs experiment the smallest increase of the vdW interaction on compression since they are located between the S3 atoms and not along the channels per se.

Other topological properties than $\rho(r)$ and its Laplacian, $\nabla^2\rho(r)$, can be considered to describe the nature of the chemical bonds such as the local energy densities, $G(r)$, $V(r)$ and $H(r)$ refering to the kinetic, potential and total energy densities, respectively. On the other hand and considering the BCPs, where $\nabla\rho(r) = 0$ and the Kirzhnits[103] approximation holds, the H_b/ρ_b, G_b/ρ_b and $|V_b|/G_b$ ratios give adimensional numbers that can be used for the chemical bonding

classification. Furthermore, these ratios allow comparing with other systems since they are intrinsic properties and not extrinsic properties as $\rho(r)$ and its Laplacian, $\nabla^2\rho(r)$.[100, 104-109] The first was introduced by Espinosa[108] and stablishes $H_b/\rho_b < 0$ for SS interactions (covalent and polar bonds) and $H_b/\rho_b > 0$ for CS interactions (ionic bonds, H-bonds and vdW interactions); the second was proposed to distinguish in a more generic way between SS interactions ($G_b/\rho_b < 1$) and CS interactions ($G_b/\rho_b > 1$).[107] Lastly, the $|V_b|/G_b$ ratio establishes three chemical bonding regions: a) a pure CS interaction ($|V_b|/G_b < 1$, $\nabla^2\rho_b > 0$); b) a pure SS interaction ($|V_b|/G_b > 2$, $\nabla^2\rho_b < 0$); and c) a transit CS interaction ($1 < |V_b|/G_b < 2$, $\nabla^2\rho_b > 0$). Therefore, knowing these density energies and their ratios we can evaluate the pressure dependence of G_b and V_b and properly characterize the different chemical bonds and their variation under compression.

Figure 11 a), b) and **c)** shows the pressure dependence of the H_b/ρ_b, G_b/ρ_b and $|V_b|/G_b$ ratios. In view of these ratios at zero pressure and having in mind **Figure 10**, we can discern the nature of the chemical bonding according to the classification scheme of **Ref.**[100] In this way, Ga-S bonds can be described as polar bonds (small ρ_b, positive $\nabla^2\rho_b$, $H_b/\rho_b < 0$, $G_b/\rho_b > 0$ and $1 < |V_b|/G_b < 2$), meanwhile S-S BCPs evidence the vdW interactions along the channels (smaller ρ_b than Ga-S BCPs, positive $\nabla^2\rho_b$, $H_b/\rho_b > 0$, $G_b/\rho_b > 0$ and $|V_b|/G_b < 1$). Among the Ga-S bonds, we can distinguish two types: Ga1(2)-S3 and Ga1(2)-S1(2) bonds. The former exhibit the highest absolute values of these ratios, the highest ρ_b and the highest $\nabla^2\rho_b$ for the Ga2-S3 and a similar $\nabla^2\rho_b$ for the Ga1-S3 in comparison to other Ga-S bonds. On other hand, Ga1(2)-S1(2) bonds exhibit intermediate absolute values of the ratios, as well as intermediate values of ρ_b and $\nabla^2\rho_b$. We must stress that using the values of ρ_b and the sign of $\nabla^2\rho_b$ as a criterion to classify the chemical bonding is critical to establish a clear difference between ionic interactions (CS) and polar bonds (SS). We can easily compare these interactions with those found in other systems, like cation-cation polar bonds in $CaAl_2Si_2$-type structures[104] or Ti-S bonds in layered TiS_2[110], and anion-anion vdW interactions in layered SnS_2[104] and TiS_2.[110]

Concerning the Ga-S bonds and their ratios under compression, their values are inside the range considered for polar Ga-S bonds. We can observe an increase of the absolute value of the H_b/ρ_b ratio due to the increase of the prevalence of V_b under compression (**Figure 11 a)**), at the same time that G_b increases (**Figure 11 b)**). However, the increase of G_b overcomes the increase of V_b for most Ga-S bonds (**Figure 11 c)**). Again, the Ga2-S3 bond stands out as an exception, where the increase of V_b is the most relevant. This explains the almost flat pressure behaviour of its Laplacian and its decrease above 16 GPa. Indeed, this fact shows that the Ga1-S3 and Ga2-S3 bonds are not equivalent and they could be related with the symmetrisation of the relative z coordinate of the Ga2 atoms at HP (see **Figure S7**), which drives to the phase transition observed in **Ref. 38**. On the other hand, since Ga-S bonds are considered as transit CS interactions ($1 < |V_b|/G_b < 2$, $\nabla^2\rho_b > 0$), the greater is the absolute value of H_b/ρ_b ratio, the more covalent and stronger is the bond.[108] In this sense, Ga1(2)-S3 bonds are more covalent and stronger than the rest of the Ga-S bonds.

More surprising are the S-S interactions and their behaviour under pressure. As was observed in Ga-S bonds, both V_b and G_b increase under compression (**Figure 11 a)** and **Figure 11 b)**), but contrary to Ga-S bonds, G_b is dominant at zero pressure, resulting in $H_b > 0$ (**Figure 11 a)**). In the same trend of Ga2-S3 bonds, the increase of V_b under compression is higher than the increase of G_b (**Figure 11 c)**) for the S-S interactions, but with $|V_b|/G_b < 1$ at 0 GPa. It is between 10 and 14 GPa where the interactions between S-S atoms change, from $H_b/\rho_b > 0$ to < 0 and

$|V_b|/G_b < 1$ to > 1. This change means an increment of the charge concentration in the channels, increasing the vdW interactions due to the decrease of S-S distances. Indeed, the increasing charge concentration in the channels might promote the phase transition observed at 16 GPa. Again, we can find an exception in the S3-S3 interactions, whose ratios are in the whole range of pressures inside the range of values attributed to vdW interactions.

Concerning the proposed dative bonds, Ga1-S1* and Ga2-S2*, they exhibit the smallest ρ_b, intermediate positive $\nabla^2\rho_b$, highest H_b/ρ_b, smaller G_b/ρ_b and $|V_b|/G_b$ compared to the other Ga-S bonds. Moreover, the trend of these properties on compression for both proposed dative bonds is not as soft as it can be seen for the other Ga-S bonds (**Figure 11 a), b)** and **c)**). Therefore, in terms of these topological properties and their pressure dependence, we can stablish differences on theses properties to tentatively assign the Ga1-S1* and Ga2-S2* bonds as dative. In order to highlight other relevant differences between covalent and dative bonds, we analysed the ELF of the α' phase. In particular, we evaluated the one-dimensional ELF profile (1D-ELF) along the Ga-S bonds in both GaS_4 tetrahedra (**Figure S26**). Thanks to the ELF, we can observe the different shell structure of atoms.[111] In an ionic compound, each maximum in the 1D-ELF corresponds to a closed shell of an atom. Conversely, along the covalent bond between two atoms, the 1D-ELF has a maximum at the centre of the bond. In our case, where polar bonds are present, the valence shells are deformed.[112] The 1D-ELF along the Ga1(2)-S3 bond is the only one that looks like different to other 1D-ELFs; however, the double LEP of S3 atoms impede them to form dative bonds with the bonded Ga. For the rest of the Ga-S bonds, the 1D-ELF does not allow us to distinguish between covalent and dative bonds existing in the α'-Ga_2S_3.

The maxima of the ELF can also be used to locate the position of the LEPs associated to the sulfur atoms. **Figure 12 a)** shows the representation of the ELF ($\eta = 0.87$) isosurface at 0 GPa, with the single and double LEPs of S1(2) and S3 atoms located inside the channels. At the ELF isosurface level chosen, we have plotted the LEPs with their respective maxima at several pressures, as can be seen in **Figure 12 b)**. As pressure increases, the volume of the single and double LEPs is reduced. This observation supports our assertion that the compressibility of the channels, and of the overall α' phase, is ruled by the compressibility of the LEPs. The shape of the LEPs also changes with pressure. In particular, the ELF maxima corresponding to the double LEP are more separated under compression. This separation is evidenced by the angle between the double LEP and the S3 atom (**Figure 13**) that increases from 118.5 to 131.6 degrees from 0 to 14 GPa, and is followed by a decrease at 16 GPa. This decrease at 16 GPa may suggest that the system undergoes an instability around this pressure which is related to the phase transition. On the other hand, the overall increase of LEP-S3-LEP angle with increasing pressure can be explained by the increasing repulsion of the S3 LEPs. The opening of the LEP-S3-LEP angle is a distortion of the S3 environment that affects to the surrounding Ga1(2) atoms. In fact, the Ga1-S3-Ga2 angle varies from 104.9 to 97.5 degrees from 0 to 16 GPa showing also a small jump between 14 and 16 GPa indicative of the instability (**Figure 13**).

In summary, QTAIM analysis of the electronic structure has allowed to explore the properties of the basin volumes. From the individual basin volumes we have obtained an averaged bulk modulus in agreement with the experimental and theoretical values reported in **Table 1**. Additionally, the pressure behaviour of the atomic charge and their charge transfer show a slight decrease in the ionicity of the compound with increasing pressure in agreement with the decrease of the LO-TO splitting of the Raman-active modes. Concerning the BCPs, both the charge density and its Laplacian, in addition with the three H_b/ρ_b, G_b/ρ_b and $|V_b|/G_b$ ratios, drives a clear classification of the Ga-S bonds and S-S interactions as polar bonds and vdW

interactions, respectively. The ELF and its isosurface has helped us locate the single and double LEPs along the channels and to visualize how anion LEPs in α'-Ga_2S_3 evolve under compression. In particular, the double LEP of S3 atoms separate with increasing pressure, distorting the environment of S3-bonded Ga1(2) atoms.

Electronic properties under compression

The electronic band structure of α'-Ga_2S_3 at 0 GPa has been already reported[87] and its behaviour at HP was partially studied by means of the electronic total density of states (EDOS).[38, 41] Specifically, both a decrease of the band gap from 1.9 to 1.6 eV between 0 and 9.3 GPa[38] and a increase of the band gap from 1.7 to 2.1 eV between 0 to 8 GPa[41] have been reported. Curiously, contradictory those results were strikingly different to those previously reported for isostructural β-Ga_2Se_3, that showed an increase of the band gap with pressure from optical absorption measurements[113] and that were supported by theoretical calculations.[74] Furthermore, those calculations additionally predicted a decrease of the direct band gap above 7.5 GPa in β-Ga_2Se_3. The unusual nonlinear behaviour of the direct band gap of β-Ga_2Se_3 was explained by a conduction band anticrossing of the two lowermost conduction bands (CBs) at the Γ point, resulting from the presence of the ordered vacancies in the structure of β-Ga_2Se_3.[74] In fact, the same behavior of the direct band gap was observed in OVCs, like $CdGa_2Se_4$,[74] $HgGa_2Se_4$,[74] $MgGa_2Se_4$[114] and $CdGa_2S_4$.[115] Therefore, it was proposed that this nonlinear behaviour must be rooted in the presence of ordered vacancies in OVCs, regardless of the composition and the structure. Consequently, on the basis of the reported contradictory data we have studied the behavior of the electronic band structure of α'-Ga_2S_3 under compression by means of theoretical calculations.

Figure 14 shows the electronic band structure together with the EDOS and partial electronic density of states (pEDOS) of α'-Ga_2S_3 at zero pressure (plotted with the SUMO package[116]). High symmetry directions in the BZ have been chosen according the Seek-path tool.[117, 118] The first BZ and its relevant high symmetry points of α'-Ga_2S_3 are shown in **Figure S27**. From the electronic band structure, we observed that the valence band (VB) shows the valence band maximum (VBM, green points) at the Γ point. Similarly, the CB minimum (CBM, red points) is also at the Γ point, thus yielding a direct band gap of 1.81 eV. Our direct band gap energy is quite similar to the reported 1.9 and 1.7 eV from **Refs. 38** and **41**, respectively. As expected for conventional DFT calculations, these theoretical direct band gaps are smaller than the experimental values that fall in the range of 2.4-3.5 eV.[14, 119]

The contribution of the atomic orbitals to the EDOS is shown in **Figure 14**. It is well known that the anion *p* (cation *s*) orbitals have a major contribution to the top (bottom) of the VB (CB) in heteropolar semiconductors. This is in agreement with our results for α'-Ga_2S_3. The VB is mainly composed by S 3*p* orbitals, specifically the high energy orbitals with the single and double LEPs, which have a strong *p* character. On the other hand, the Ga 4*s*, 3*d* and S 3*p* orbitals contribute equally to the CB. The contribution of the atomic orbitals of S1, S2, S3, Ga1 and Ga2 atomic to the pEDOS at 0 GPa is shown in **Figure S28 a)**. The top of the VB is mainly contributed by S3 3p orbitals, exhibiting a higher contribution of the double LEPs of the S3 atoms over the single LEPs of S1(2) atoms. On the other hand, the bottom of the CB has dominant contributions from Ga 4s and S 3p orbitals and the topmost of the CB is mainly contributed by Ga 4p orbitals and S 3p orbitals.

The theoretical pressure dependence of the direct and indirect band gap of the α'-Ga_2S_3 is shown in **Figure 15 a)**. The behaviour of the direct band gap under HP resembles quite well to that observed in other OVCs, especially in β-Ga_2Se_3:[74, 113] It increases up to around 7.5 GPa, and then decreases above that pressure. Concerning the direct-to-indirect band gap crossover, it occurs at around 5.5 GPa in α'-Ga_2S_3. A similar direct-to-indirect band gap crossover was also predicted to occur around 6.0 GPa in β-Ga_2Se_3.[74] **Figure 15 b)** depicts the pressure dependence of the VBM and the lowest three CBs at the Γ point, together the lowest CBM at the V_2' point. We can clearly observe the direct-to indirect band gap crossover near 5.5 GPa and the conduction band anticrossing at the Γ point at around 7.5 GPa. It is curious that both α'-Ga_2S_3 and β-Ga_2Se_3 pass through the same changes in their band gap at similar pressures (**Figure 15 a)** and **Figure 4 a)** of **Ref. 74**), despite the difference of the anion and that the nature of the indirect band gap and its pressure dependence are different. Finally, concerning the theoretical pressure dependence of the band gap in α'-Ga_2S_3 reported in **Ref. 38**, we think that the pressure behavior reported in **Ref. 38** likely corresponds to the indirect band gap (see **Figure 15 a)**), which seems to be more underestimated within LDA[38] than with our GGA-PBEsol calculations. On the other hand, the pressure dependence of the band gap reported up to 8 GPa in **Ref. 41** is quite similar to our results because of the use the GGA functional. However, they have not reported neither the direct-to-indirect band gap crossover at around 5.5 GPa nor the decrease of the direct band gap above 8 GPa showed in **Figure 15 a)**. In this context, we think that the reason why we have observed the indirect band gap is because we have used the complex k path suggested by the Seek-path tool[117, 118] to calculate the complex electronic band structure of the monoclinic Cc phase instead of the simple path used in the Materials Project Database.[87]

In order to quantitatively analyze the changes of the topmost VB and lowermost CBs, we have tabulated the relative pressure coefficients for the band energies, yielding 8.1, 6.0, 3.9 and 3.0 GPa^{-1} for the 1st VB, 1st and 2nd CB at the Γ point and 1st CB at the V_2' point, respectively. In view of these relative pressure coefficients, the energy of the 1st VB at the Γ point (VBM) is the most sensitive under compression. This should not be surprising since the single and double LEPs occupy the high energy levels of the VB. At increasing pressure, the closing of the channels increases the repulsion of the LEPs, especially among those of the double LEPs, driving a strong increase of the VBM energy. We must also stress the larger relative pressure coefficients of the 1st and 2nd CB at the Γ point in comparison to that of the 1st CB at the V_2' point leads to the direct-to-indirect band gap crossover at 5.5 GPa. In the same way, the larger relative pressure coefficient of the 1st in comparison with the 2nd CB at the Γ point leads to the anticrossing of the two lowermost CB bands of the direct band gap near 7.5 GPa, thus resulting in a change of pressure coefficient for the direct band gap at this pressure. In summary, our results for α'-Ga_2S_3 show a nonlinear pressure dependence of the direct band gap in good agreement with the expected behavior for all OVCs, as first stated in **Ref. 74**.

The electronic band structure at 6 GPa is shown in **Figure S29** to evidence the indirect band gap Γ-V_2' on α'-Ga_2S_3. A more detailed view of the pEDOS at 6 GPa of **Figure S29** is illustrated **Figure S28 b)** for each atom. We can observe a more distribuited contribution of Ga 4*s*, 3*d* and 4*p* orbitals throughout the CB, as S 3*s* and 3*p* orbitals do. This important contribution is more remarkable at 16 GPa (**Figure S28 c)**), where the atomic orbitals from Ga and S atoms are more equally distributed over the CB.

As noted above, the most sensitive pressure behaviour of the VBM is rooted in the strong repulsion of the LEPs located in the channels, as a consequence of their approach with increasing

pressure. According to **Figure 5 c)** and **d)**, the Ga-S bond compressibilities decay to a greater extent (except for the Ga1-S1* bond) below 7.5 GPa. At the same time, the charge transfers decrease smoothly (**Figure S24 c)**) as a consequence of the increased covalent nature and strength of the Ga-S bonds (**Figure 11 a)** and **c)**) under compression. Moreover, the repulsion between the LEPs of the S3 atoms is moderate below 7.5 GPa (**Figure 13**). Therefore, it is around 7.5 GPa where various changes in the trends mentioned are observed. These results allow us to tentatively suggest that the nonlinear pressure dependence of the direct band gap near 7.5 GPa could be related to the slight decrease of the compressibilities, as a result of the prevalence of the repulsive forces between the nuclei, and the increase of the vdW interactions along the channels (**Figure 11 a)** and **c)**). These latter are caused by the higher increase of the repulsion between the LEPs of the S3 atoms as a consequence of the closing of the channels.

In summary, we have reported in this section the pressure dependence of the direct and indirect band gaps of α'-Ga_2S_3. Our results evidence a clear similarity between the behaviour of the electronic band structure of α'-Ga_2S_3 under compression and those of other OVCs, especially with isostructural β-Ga_2Se_3. In particular, we have found a nonlinear behavior of the direct band gap and a direct-to-indirect band gap crossover, as in β-Ga_2Se_3. This similarity was not reported in two previous works that also analysed the electronic band structure of α'-Ga_2S_3 under compression. Additionally, we have emphasized the role of the anion LEPs, contributing mainly to the topmost VB, in the changes of the electronic band structure of α'-Ga_2S_3 under compression.

Conclusions

In this work, we have performed HP-XRD, HP-RS and HT-RS measurements on α'-Ga_2S_3, in addition to *ab initio* calculations. With our experimental HP-XRD measurements and theoretical results, we have revised the pressure dependence of the volume and lattice parameters of α'-Ga_2S_3 in comparison with previously data.[38] In particular, we have shown that the unit-cell volume vs. pressure is better fitted to a BM3-EoS, with a softer behaviour under compression than previously reported[38] and in agreement with the pressure behaviour β-Ga_2Se_3.[79] We have reported the isothermal compressibility tensor between 0 and 14 GPa and its principal axes with the maximum, minimum and intermediate compressibilities and their relation with the channels of the structure. In particular, the maximum and intermediate compressibilities are related to the cross-sections of the channels. The role of the channels in the anisotropic pressure behaviour of the unit cell is highlighted. In particular, we have found that the channel compressibility governs the unit-cell volume compressibility and that the two GaS_4 tetrahedra become more distorted at increasing pressure, with the distortion of both tetrahedra being equal at 16 GPa. This result, in addition to the symmetrisation of the z coordinate of Ga2 atoms, points out to the pressure induced phase transition observed at 16 GPa, as already reported in **Ref. 38** and **41**.

HP-RS measurements in α'-Ga_2S_3 have allowed us to tentatively assign the symmetries of the observed Raman-active modes, to give the pressure coefficients of the Raman-active modes and to reveal structural changes above 15.1 GPa, in agreement with the pressure-induced phase transition reported previously.[38, 41] Besides, HT-RS measurements have shown the thermal stability until reaching the melting point at about 1300 K. Our lattice-dynamic calculations and the Lucazeau's idealized model[78] have allowed us to assign the symmetry of most of the observed Raman modes. Additionally, our calculations have lead us to highlight the mixed bending-stretching character of the Raman-active modes, with a remarkable vibration

amplitude of Ga and S1 and S2 (S3) atoms in the low-frequency region and lower (high) part of the high-frequency region, respectively. The anharmonic effects of the different experimentally observed Raman modes have been studied, showing their different cubic and quartic anharmonic contributions, with a predominance of the implicit effect in most modes. In particular, the *A'*(6) mode, the breathing mode related to the vacancies, has the highest anharmonicity and cubic anharmonic contribution at HP and HT, respectively.

The study of the topology of the electron density at HP within the QTAIM method has allowed us to explore the properties of the basin volumes and confirm the bulk modulus as well the increase of the covalency (decrease of the ionicity) of the compound with increasing pressure. Additionally, it has allowed us to classify the different chemical bonds in the structure and has evidenced the strengthening of the Ga-S bonds at increasing pressure and the increase of the vdW interactions along the channels, especially above 10 GPa. On the other hand, we have tentatively assigned the Ga1-S1* and Ga2-S2* bonds as dative bonds attending to the notable differences in bond lengths, compressibilities and topological properties of these two bonds with respect to the other Ga-S bonds. Thanks to the ELF, we have visually evaluated the decreasing volume of single and double LEPs and the increasing angle between the double LEPs of the S3 atoms at HP. This angle shows a decrease around 16 GPa that may suggest an incipient instability related to the first-order phase transition already commented. Moreover, we have presented the use of the topological properties as ρ_b, $\nabla^2\rho_b$ and the H_b/ρ_b, G_b/ρ_b and $|V_b|/G_b$ ratios as an easy methodology to evaluate the chemical interactions within a system and enabling the comparison with others, in addition to studying the pressure dependence of these interactions.

Finally, our calculated electronic band structures at HP have evidenced a strong nonlinear pressure behaviour of the direct band gap and a pressure-induced direct-to-indirect band gap crossover. Both features are similar to those previously reported for isostructural β-Ga_2Se_3 and other OVCs. Moreover, we have shown that, as in other OVCs, the VBM in α'-Ga_2S_3 shows a very large pressure coefficient that is related to the strong contribution of anionic LEPs. In this context, there is a greater relevance for the topmost VB of the double anion LEPs in α'-Ga_2S_3 than in less complex OVCs. In α'-Ga_2S_3, the strong compression of the anion LEPs leads to a strong increase of the VBM energy so LEPs play a similar role as in adamantine-based OVCs, like $CdGa_2S_4$. The strong compression of these LEPs explains the strong increase of the VBM energy and the nonlinear dependence of the direct band gap.

In summary, the present work has been aimed at understanding in detail the behaviour of the low-pressure phase of α'-Ga_2S_3 under compression. Our study has shown that the HP properties of α'-Ga_2S_3 are similar to those of β-Ga_2Se_3 and other adamantine-based OVCs. Therefore, this work has contributed to stablish a general behaviour under compression of materials with unpaired anion electrons in the crystalline structure.

Acknowledgements

The authors thank the financial support from Spanish Research Agency (AEI) under projects MALTA Consolider Team network (RED2018-102612-T) and projects MAT2016-75586-C4-2/3-P, FIS2017-83295-P, PID2019-106383GB-42/43, and PGC2018-097520-A-100, as well as from Generalitat Valenciana under Project PROMETEO/2018/123 (EFIMAT). A. M., and P. R.-H acknowledge computing time provided by Red Española de Supercomputación (RES) and MALTA-Cluster and E.L.D.S. acknowledges Marie Sklodowska-Curie Grant No. 785789-COMEX

from the European Union's Horizon 2020 research and innovation program. J. A. S. also wants to thank the Ramon y Cajal fellowship (RYC-2015-17482) for financial support. We also thank ALBA synchrotron light source for funded experiment 2017022088 at the MSPD-BL04 beamline.

References

(1) Wang, J.; Yuan, W.; Li, M. Thermodynamic modeling of the Ga–N–Na system. *Journal of crystal growth* **2007**, *307*, 59-65.

(2) Okamoto, H.; Massalski, T. Thermodynamically improbable phase diagrams. *Journal of phase equilibria* **1991**, *12*, 148-168.

(3) Pelton, A.; Larose, S. The Ga-Na (Gallium-Sodium) System. *Bulletin of Alloy Phase Diagrams* **1990**, *11*, 347-353.

(4) Okamoto, H. Ga-Na (Gallium-Sodium). *Journal of Phase Equilibria and Diffusion* **2010**, *31*, 206-206.

(5) Wang, P.; Liu, M.; Mo, F.; Long, Z.; Fang, F.; Sun, D.; Zhou, Y.-N.; Song, Y. Exploring the Sodium Ion Storage Mechanism of Gallium Sulfide (Ga_2S_3): A Combined Experimental and Theoretical Approach. *Nanoscale* **2019**.

(6) Ni, Y.; Wu, H.; Wang, Z.; Mao, M.; Cheng, G.; Fei, H. Synthesis and growth of nonlinear infrared crystal material $AgGeGaS_4$ via a new reaction route. *Journal of crystal growth* **2009**, *311*, 1404-1406.

(7) Isaenko, L.; Vasilyeva, I.; Merkulov, A.; Yelisseyev, A.; Lobanov, S. Growth of new nonlinear crystals $LiMX_2$ (M= Al, In, Ga; X= S, Se, Te) for the mid-IR optics. *Journal of crystal growth* **2005**, *275*, 217-223.

(8) Kim, Y.; Seo, I.-s.; Martin, S. W.; Baek, J.; Shiv Halasyamani, P.; Arumugam, N.; Steinfink, H. Characterization of new infrared nonlinear optical material with high laser damage threshold, $Li_2Ga_2GeS_6$. *Chemistry of Materials* **2008**, *20*, 6048-6052.

(9) Bai, L.; Lin, Z.; Wang, Z.; Chen, C.; Lee, M.-H. Mechanism of linear and nonlinear optical effects of chalcopyrite $AgGaX_2$ (X= S, Se, and Te) crystals. *The Journal of chemical physics* **2004**, *120*, 8772-8778.

(10) Bai, L.; Lin, Z.; Wang, Z.; Chen, C. Mechanism of linear and nonlinear optical effects of chalcopyrites $LiGaX_2$ (X= S, Se, and Te) crystals. *J. Appl. Phys.* **2008**, *103*, 083111.

(11) Zhang, M.-J.; Jiang, X.-M.; Zhou, L.-J.; Guo, G.-C. Two phases of Ga_2S_3: promising infrared second-order nonlinear optical materials with very high laser induced damage thresholds. *J. Mater. Chem. C* **2013**, *1*, 4754-4760.

(12) El Shaikh, H.; Abdal-Rahman, M.; Belal, A.; Ashraf, I. Photoconductivity studies of gallium sesquisulphide single crystals. *J. Phys. D: Appl. Phys.* **1996**, *29*, 466.

(13) Kim, W.-T.; Kim, H.-S.; Kim, Y.-G.; Hahn, S.-R. Optical energy gaps of $In_{2-x}Ga_xS_3$ thin films prepared by spray pyrolysis. *Journal of materials science letters* **1987**, *6*, 479-480.

(14) Yoon, C.-S.; Medina, F.; Martinez, L.; Park, T.-Y.; Jin, M.-S.; Kim, W.-T. Blue photoluminescence of α-Ga_2S_3 and α-Ga_2S_3:Fe^{2+} single crystals. *Appl. Phys. Lett.* **2003**, *83*, 1947-1949.

(15) Ren, J.; Li, B.; Yang, G.; Xu, W.; Zhang, Z.; Secu, M.; Bercu, V.; Zeng, H.; Chen, G. Broadband near-infrared emission of chromium-doped sulfide glass-ceramics containing Ga_2S_3 nanocrystals. *Optics letters* **2012**, *37*, 5043-5045.

(16) Sastry, I.; Bacalski, C.; McKittrick, J. Preparation of Green-Emitting $Sr_{1-x}Eu_xGa_2S_4$ Phosphors by a Solid-State Rapid Metathesis Reaction. *Journal of The Electrochemical Society* **1999**, *146*, 4316-4319.

(17) Aono, T.; Kase, K. Green photoemission of α-Ga_2S_3 crystals. *Solid state communications* **1992**, *81*, 303-305.

(18) Ho, C.-H.; Chen, H.-H. Optically decomposed near-band-edge structure and excitonic transitions in Ga_2S_3. *Scientific reports* **2014**, *4*, 6143.

(19) Al Garni, S.; Qasrawi, A. Design and characterization of the Ge/Ga_2S_3 heterojunction. *Journal of Electronic Materials* **2017**, *46*, 4848-4856.
(20) Kokh, K. A.; Huang, Z.-M.; Huang, J.-G.; Gao, Y.-Q.; Uralbekov, B.; Panomarev, J.; Lapin, I.; Svetlichnyi, V.; Lanskii, G.; Andreev, Y. M. Study of Ga_2S_3 crystals grown from melt and PbCl2 flux. *Mater. Res. Bull.* **2016**, *84*, 462-467.
(21) Huang, Z.; Huang, J.-G.; Kokh, K.; Svetlichnyi, V.; Shabalina, A.; Andreev, Y. M.; Lanskii, G. In *Ga_2S_3: Optical properties and perspectives for THz applications*, Infrared, Millimeter, and Terahertz waves (IRMMW-THz), 2015 40th International Conference on, 2015; IEEE: 2015; pp 1-2.
(22) Jastrzebski, C.; Jastrzebski, D. J.; Kozak, V.; Pietak, K.; Wierzbicki, M.; Gebicki, W. Synthesis and structural characterization of microcrystalline Ga_2S_3 layers on a GaP semiconductor substrate. *Materials Science in Semiconductor Processing* **2019**, *94*, 80-85.
(23) Zervos, M.; Othonos, A.; Gianneta, V.; Travlos, A.; Nassiopoulou, A. G. Sn doped β-Ga_2O_3 and β-Ga_2S_3 nanowires with red emission for solar energy spectral shifting. *J. Appl. Phys.* **2015**, *118*, 194302.
(24) Alharbi, S.; Qasrawi, A. Dielectric dispersion in Ga_2S_3 thin films. *Plasmonics* **2017**, *12*, 1045-1049.
(25) Ho, C.-H.; Lin, M.-H.; Wang, Y.-P.; Huang, Y.-S. Synthesis of In_2S_3 and Ga_2S_3 crystals for oxygen sensing and UV photodetection. *Sensors and Actuators A: Physical* **2016**, *245*, 119-126.
(26) Wang, L.; Tu, C. Growth modulation of Ga_2S_3 horizontal nanowires and its optical properties. *Nanotechnology* **2020**, *31*, 165603.
(27) Hu, Z. M.; Fei, G. T.; De Zhang, L. Synthesis and tunable emission of Ga_2S_3 quantum dots. *Materials Letters* **2019**, *239*, 17-20.
(28) Pardo, M.; Guittard, M.; Chilouet, A.; Tomas, A. Diagramme de phases gallium-soufre et études structurales des phases solides. *J. Solid State Chem.* **1993**, *102*, 423-433.
(29) Lieth, R.; Heijligers, H.; vd Heijden, C. The P-T-X Phase Diagram of the System Ga-S. *Journal of the Electrochemical Society* **1966**, *113*, 798-801.
(30) Guymont, M.; Tomas, A.; Pardo, M.; Guittard, M. Electron microscope study of γ-Ga_2S_3. *phys. status solidi (a)* **1989**, *113*, K5-K7.
(31) Gallego-Parra, S.; Gomis, O.; Vilaplana, R.; Ortiz, H. M.; Perez-Gonzalez, E.; Luna, R.; Rodríguez-Hernández, P.; Muñoz, A.; Ursaki, V.; Tiginyanu, I. Vibrational properties of $CdGa_2S_4$ at high pressure. *J. Appl. Phys.* **2019**, *125*, 115901.
(32) Manjon, F. J.; Gomis, O. In *Pressure-Induced Phase Transitions in AB_2X_4 Chalcogenide Compounds*; Manjon, F. J., Tiginyanu, I. M., Ursaki, V., Ed.; Springer: Berlin, 2013; Chapter *AB_2Se_4* Ordered-Vacancy Compounds at High Pressures, Vol. 189, pp 163-184.
(33) Manjon, F. J.; Vilaplana, R. In *Pressure-Induced Phase Transitions in AB_2X_4 Chalcogenide Compounds*; Manjon, F. J., Tiginyanu, I. M., Ursaki, V. V., Ed.; Springer: Berlin, 2013; Chapter *AB_2S_4* Ordered-Vacancy Compounds at High Pressures, Vol. 189, pp 133-161.
(34) Tomas, A.; Guymont, M.; Pardo, M.; Guittard, M.; Flahaut, J. X-ray diffraction and electron microscopy studies of α-and β-Ga_2S_3. *phys. status solidi (a)* **1988**, *107*, 775-784.
(35) Gillespie, a. R.; Nyholm, R. Inorganic stereochemistry. *Quarterly Reviews, Chemical Society* **1957**, *11*, 339-380.
(36) Goodyear, J.; Steigmann, G. The crystal structure of α-Ga_2S_3. *Acta Crystallographica* **1963**, *16*, 946-949.
(37) Jones, C.; Bryan, J.; Kirschbaum, K.; Edwards, J. Refinement of the crystal structure of digallium trisulfide, Ga_2S_3. *Zeitschrift für Kristallographie-New Crystal Structures* **2001**, *216*, 349-350.
(38) Lai, X.; Zhu, F.; Qin, S.; Chen, D.; Li, Y.; Yang, K.; Wu, X. Experimental and theoretical identification of a high-pressure polymorph of Ga_2S_3 with α-Bi_2Te_3-type structure. *J. Appl. Phys.* **2014**, *116*, 193507.

(39) Vilaplana, R.; Parra, S. G.; Jorge-Montero, A.; Rodríguez-Hernández, P.; Munoz, A.; Errandonea, D.; Segura, A.; Manjón, F. J. Experimental and theoretical studies on α-In_2Se_3 at high pressure. *Inorganic chemistry* **2018**, *57*, 8241-8252.
(40) Manjón, F.; Vilaplana, R.; Gomis, O.; Pérez-González, E.; Santamaría-Pérez, D.; Marín-Borrás, V.; Segura, A.; González, J.; Rodríguez-Hernández, P.; Muñoz, A. High-pressure studies of topological insulators Bi_2Se_3, Bi_2Te_3, and Sb_2Te_3. *phys. status solidi (b)* **2013**, *250*, 669-676.
(41) Yang, L.; Jiang, J.; Dai, L.; Hu, H.; Hong, M.; Zhang, X.; Li, H.; Liu, P. High-pressure structural phase transition and metallization in Ga2S3 under non-hydrostatic and hydrostatic conditions up to 36.4 GPa. *J. Mater. Chem. C* **2021**.
(42) Pereira, A. L.; Sans, J. A.; Vilaplana, R.; Gomis, O.; Manjón, F.; Rodriguez-Hernandez, P.; Muñoz, A.; Popescu, C.; Beltrán, A. Isostructural second-order phase transition of β-Bi_2O_3 at high pressures: an experimental and theoretical study. *The Journal of Physical Chemistry C* **2014**, *118*, 23189-23201.
(43) Cuenca-Gotor, V. P.; Sans, J. Á.; Gomis, O.; Mújica, A.; Radescu, S.; Munoj, A.; Rodriguez-Hernadez, P.; Da Silva, E. L.; Popescu, C.; Ibañez, J.; Vilaplana, R.; Manjon, F. J. Orpiment under compression: metavalent bonding at high pressure. *Phys. Chem. Chem. Phys.* **2020**.
(44) Efthimiopoulos, I.; Kemichick, J.; Zhou, X.; Khare, S. V.; Ikuta, D.; Wang, Y. High-pressure studies of Bi_2S_3. *The Journal of Physical Chemistry A* **2014**, *118*, 1713-1720.
(45) Xu, M.; Jakobs, S.; Mazzarello, R.; Cho, J.-Y.; Yang, Z.; Hollermann, H.; Shang, D.; Miao, X.; Yu, Z.; Wang, L. Impact of Pressure on the Resonant Bonding in Chalcogenides. *The Journal of Physical Chemistry C* **2017**, *121*, 25447-25454.
(46) Walsh, A.; Payne, D. J.; Egdell, R. G.; Watson, G. W. Stereochemistry of post-transition metal oxides: revision of the classical lone pair model. *Chemical Society Reviews* **2011**, *40*, 4455-4463.
(47) Gomis, O.; Vilaplana, R.; Manjón, F. J.; Pérez-González, E.; López-Solano, J.; Rodríguez-Hernández, P.; Muñoz, A.; Errandonea, D.; Ruiz-Fuertes, J.; Segura, A.; Santamaria-Pérez, D.; Tiginyanu, I. M.; Ursaki, V. High-pressure optical and vibrational properties of $CdGa_2Se_4$: Order-disorder processes in adamantine compounds. *J. Appl. Phys.* **2012**, *111*, 013518.
(48) Gibbs, G. V.; Wallace, A. F.; Downs, R.; Ross, N. L.; Cox, D. F.; Rosso, K. M. Thioarsenides: a case for long-range Lewis acid–base-directed van der Waals interactions. *Physics and Chemistry of Minerals* **2011**, *38*, 267-291.
(49) Hejny, C.; Sagl, R.; Többens, D. M.; Miletich, R.; Wildner, M.; Nasdala, L.; Ullrich, A.; Balic-Zunic, T. Crystal-structure properties and the molecular nature of hydrostatically compressed realgar. *Physics and Chemistry of Minerals* **2012**, *39*, 399-412.
(50) Vaidya, S.; Kennedy, G. Compressibility of 22 elemental solids to 45 KB. *J. Phys. Chem. Solids* **1972**, *33*, 1377-1389.
(51) Lepore, G.; Ballaran, T. B.; Nestola, F.; Bindi, L.; Pasqual, D.; Bonazzi, P. Compressibility of β-As_4S_4: an in situ high-pressure single-crystal X-ray study. *Mineralogical Magazine* **2012**, *76*, 963-973.
(52) Tuktabiev, M.; Popova, S.; Brazhkin, V.; Lyapin, A.; Katayama, Y. Compressibility and polymorphism of α-As_4S_4 realgar under high pressure. *J. Phys.: Condens. Matter* **2009**, *21*, 385401.
(53) Chattopadhyay, T.; Werner, A.; Schnering, H. Thermal expansion and compressibility of β-As_4S_3. *J. Phys. Chem. Solids* **1982**, *43*, 919-923.
(54) Klotz, S.; Chervin, J. C.; Munsch, P.; Le Marchand, G. Hydrostatic limits of 11 pressure transmitting media. *J. Phys. D: Appl. Phys.* **2009**, *42*, 075413.
(55) Dewaele, A.; Loubeyre, P.; Mezouar, M. Equations of state of six metals above 94 GPa. *Physical review B* **2004**, *70*, 094112.
(56) Fauth, F.; Peral, I.; Popescu, C.; Knapp, M. The new material science powder diffraction beamline at ALBA synchrotron. *Powder Diffraction* **2013**, *28*, S360-S370.
(57) Prescher, C.; Prakapenka, V. B. DIOPTAS: a program for reduction of two-dimensional X-ray diffraction data and data exploration. *High Pressure Research* **2015**, *35*, 223-230.

(58) Toby, B. H.; Von Dreele, R. B. GSAS-II: the genesis of a modern open-source all purpose crystallography software package. *Journal of Applied Crystallography* **2013**, *46*, 544-549.
(59) Mao, H. K.; Xu, J. A.; Bell, P. M. Calibration of the ruby pressure gauge to 800 kbar under quasi-hydrostatic conditions. *Journal of Geophysical Research: Solid Earth* **1986**, *91*, 4673-4676.
(60) Hohenberg, P.; Kohn, W. Inhomogeneous electron gas. *Physical review* **1964**, *136*, B864.
(61) Kresse, G.; Hafner, J. Ab initio molecular dynamics for liquid metals. *Physical Review B* **1993**, *47*, 558.
(62) Blöchl, P. E. Projector augmented-wave method. *Physical review B* **1994**, *50*, 17953.
(63) Kresse, G.; Joubert, D. From ultrasoft pseudopotentials to the projector augmented-wave method. *Physical review b* **1999**, *59*, 1758.
(64) Perdew, J. P.; Ruzsinszky, A.; Csonka, G. I.; Vydrov, O. A.; Scuseria, G. E.; Constantin, L. A.; Zhou, X.; Burke, K. Restoring the density-gradient expansion for exchange in solids and surfaces. *Physical Review Letters* **2008**, *100*, 136406.
(65) Parlinski, K. Computer Code Phonon. see: http://www.computingformaterials.com/index.html
(66) Otero-de-la-Roza, A.; Johnson, E. R.; Luaña, V. Critic2: A program for real-space analysis of quantum chemical interactions in solids. *Computer Physics Communications* **2014**, *185*, 1007-1018.
(67) Yu, M.; Trinkle, D. R. Accurate and efficient algorithm for Bader charge integration. *The Journal of chemical physics* **2011**, *134*, 064111.
(68) K. Dewhurst; S. Sharma Elk code. *The Elk FP-LAPW code*, http://elk.sourceforge.net/
(69) Kirzhnits, D. Quantum corrections to the Thomas-Fermi equation. *Soviet Phys. JETP* **1957**, *5*.
(70) Kirzhnits, D. A. Field theoretical methods in many-body systems. *American Journal of Physics* **1967**, *35*, 1166-1167.
(71) Momma, K.; Izumi, F. VESTA 3 for three-dimensional visualization of crystal, volumetric and morphology data. *Journal of Applied Crystallography* **2011**, *44*, 1272-1276.
(72) Gonzalez-Platas, J.; Alvaro, M.; Nestola, F.; Angel, R. EosFit7-GUI: a new graphical user interface for equation of state calculations, analyses and teaching. *Journal of Applied Crystallography* **2016**, *49*, 1377-1382.
(73) Takumi, M.; Koshio, Y.; Nagata, K. X-Ray, Raman and Photoluminescence Study of Vacancy Ordered β-Ga_2Se_3 under High Pressure. *phys. status solidi (b)* **1999**, *211*, 123-129.
(74) Manjón, F. J.; Gomis, O.; Rodríguez-Hernández, P.; Pérez-González, E.; Muñoz, A.; Errandonea, D.; Ruiz-Fuertes, J.; Segura, A.; Fuentes-Cabrera, M.; Tiginyanu, I. M.; Ursaki, V. Nonlinear pressure dependence of the direct band gap in adamantine ordered-vacancy compounds. *Physical Review B* **2010**, *81*, 195201.
(75) Sans, J. A.; Vilaplana, R.; da Silva, E. L.; Popescu, C.; Cuenca-Gotor, V. P.; Andrada-Chacón, A. n.; Sánchez-Benitez, J.; Gomis, O.; Pereira, A. L.; Rodríguez-Hernández, P. Characterization and Decomposition of the Natural van der Waals $SnSb_2Te_4$ under Compression. *Inorganic Chemistry* **2020**.
(76) Cliffe, M. J.; Goodwin, A. L. PASCal: a principal axis strain calculator for thermal expansion and compressibility determination. *Journal of Applied Crystallography* **2012**, *45*, 1321-1329.
(77) Landau, L. D.; Kosevich, A.; Pitaevskii, L. P.; Lifshitz, E. M. Theory of elasticity. **1986**.
(78) Lucazeau, G.; Leroy, J. Etude vibrationnelle de α Ga_2S_3. *Spectrochimica Acta Part A: Molecular Spectroscopy* **1978**, *34*, 29-32.
(79) Miller, A.; MacKinnon, A.; Weaire, D. In *Solid state physics*; Elsevier: 1982; Vol. 36, pp 119-175.
(80) Julien, C.; Barnier, S.; Ivanov, I.; Guittard, M.; Pardo, M.; Chilouet, A. Vibrational studies of copper thiogallate solid solutions. *Materials Science and Engineering: B* **1999**, *57*, 102-109.
(81) Barnier, S.; Palazzi, M.; Massot, M.; Julien, C. Vibrational spectra of the vitreous Ga_2S_3-Na_2S system. *Solid State Ionics* **1990**, *44*, 81-86.

(82) Julien, C.; Barnier, S.; Massot, M.; Pardo, M. Vibrational studies of solid solutions formed in the gallium-cadmium-sulphur system. *Mater. Res. Bull.* **1994**, *29*, 785-794.
(83) Ursaki, V. V.; Burlakov, I. I.; Tiginyanu, I. M.; Raptis, Y. S.; Anastassakis, E.; Anedda, A. Phase transitions in defect chalcopyrite compounds under hydrostatic pressure. *Physical Review B* **1999**, *59*, 257.
(84) Vilaplana, R.; Robledillo, M.; Gomis, O.; Sans, J. A.; Manjón, F. J.; Pérez-González, E.; Rodríguez-Hernández, P.; Muñoz, A.; Tiginyanu, I. M.; Ursaki, V. V. Vibrational study of $HgGa_2S_4$ under high pressure. *J. Appl. Phys.* **2013**, *113*, 093512.
(85) Taylor, M. J. Raman and infrared spectra and vibrational assignments of gallium (II) sulphide. *J. Raman Spectrosc.* **1973**, *1*, 355-358.
(86) Friedrich, D.; Schlosser, M.; Weihrich, R.; Pfitzner, A. Polymorphism of $CsGaS_2$–structural characterization of a new two-dimensional polymorph and study of the phase-transition kinetics. *Inorganic Chemistry Frontiers* **2017**, *4*, 393-400.
(87) Jain, A.; Ong, S. P.; Hautier, G.; Chen, W.; Richards, W. D.; Dacek, S.; Cholia, S.; Gunter, D.; Skinner, D.; Ceder, G. Commentary: The Materials Project: A materials genome approach to accelerating materials innovation. *Apl Materials* **2013**, *1*, 011002.
(88) Cheng, Y. C.; Jin, C. Q.; Gao, F.; Wu, X. L.; Zhong, W.; Li, S. H.; Chu, P. K. Raman scattering study of zinc blende and wurtzite ZnS. *J. Appl. Phys.* **2009**, *106*, 123505.
(89) Abstreiter, G.; Cardona, M.; Pinczuk, A. In *Light Scattering in Solids IV*; Springer: 1984; pp 5-150.
(90) Ahamad, T.; Alshehri, S. M. In *Green Synthesis and Characterization of Gallium (III) Sulphide (α-Ga_2S_3) Nanoparicles at Room Temperature*, Nano Hybrids, 2014; Trans Tech Publ: 2014; pp 37-46.
(91) Miller, S. A.; Gorai, P.; Ortiz, B. R.; Goyal, A.; Gao, D.; Barnett, S. A.; Mason, T. O.; Snyder, G. J.; Lv, Q.; Stevanović, V. Capturing anharmonicity in a lattice thermal conductivity model for high-throughput predictions. *Chemistry of Materials* **2017**, *29*, 2494-2501.
(92) Link, A.; Bitzer, K.; Limmer, W.; Sauer, R.; Kirchner, C.; Schwegler, V.; Kamp, M.; Ebling, D.; Benz, K. Temperature dependence of the E2 and A1(LO) phonons in GaN and AlN. *J. Appl. Phys.* **1999**, *86*, 6256-6260.
(93) Zallen, R.; Conwell, E. The effect of temperature on libron frequencies in molecular crystals: Implications for TTF-TCNQ. *Solid State Communications* **1979**, *31*, 557-561.
(94) Weinstein, B. A.; Zallen, R. In *Light Scattering in Solids IV*; Springer: 1984; pp 463-527.
(95) Bhatt, S. V.; Deshpande, M.; Sathe, V.; Rao, R.; Chaki, S. Raman spectroscopic investigations on transition-metal dichalcogenides MX_2 (M= Mo, W; X= S, Se) at high pressures and low temperature. *J. Raman Spectrosc.* **2014**, *45*, 971-979.
(96) Besson, J.; Cernogora, J.; Slade, M.; Weinstein, B.; Zallen, R. Pressure effects on the absorption edge, refractive index, and Raman spectra of crystalline and amorphous As_2S_3. *Physica B+C* **1981**, *105*, 319-323.
(97) Jakšić, Z. Temperature and pressure dependence of phonon frequencies in GeS_2, $GeSe_2$, and $SnGeS_3$. *phys. status solidi (b)* **2003**, *239*, 131-143.
(98) Efthimiopoulos, I.; Berg, M.; Bande, A.; Puskar, L.; Ritter, E.; Xu, W.; Marcelli, A.; Ortolani, M.; Harms, M.; Müller, J. Effects of temperature and pressure on the optical and vibrational properties of thermoelectric SnSe. *Phys. Chem. Chem. Phys.* **2019**, *21*, 8663-8678.
(99) Bader, R., A Quantum Theory, Clarendon. In Oxford: 1990.
(100) Gatti, C. Chemical bonding in crystals: new directions. *Zeitschrift für Kristallographie-Crystalline Materials* **2005**, *220*, 399-457.
(101) Pendás, A. M.; Costales, A.; Blanco, M.; Recio, J.; Luaña, V. Local compressibilities in crystals. *Physical Review B* **2000**, *62*, 13970.
(102) Mori-Sánchez, P.; Pendás, A. M.; Luaña, V. A classification of covalent, ionic, and metallic solids based on the electron density. *Journal of the American Chemical Society* **2002**, *124*, 14721-14723.

(103) Yang, H.; Boulet, P.; Record, M.-C. A rapid method for analyzing the chemical bond from energy densities calculations at the bond critical point. *Computational and Theoretical Chemistry* **2020**, 112784.
(104) Zhang, J.; Song, L.; Sist, M.; Tolborg, K.; Iversen, B. B. Chemical bonding origin of the unexpected isotropic physical properties in thermoelectric Mg_3Sb_2 and related materials. *Nature communications* **2018**, *9*, 4716.
(105) Bianchi, R.; Gervasio, G.; Marabello, D. Experimental electron density analysis of $Mn_2(CO)_{10}$: metal− metal and metal− Ligand bond characterization. *Inorganic chemistry* **2000**, *39*, 2360-2366.
(106) Yang, H.; Boulet, P.; Record, M.-C. New insight into the structure-property relationships from chemical bonding analysis: Application to thermoelectric materials. *J. Solid State Chem.* **2020**, *286*, 121266.
(107) Bader, R. F.; Essén, H. The characterization of atomic interactions. *The Journal of chemical physics* **1984**, *80*, 1943-1960.
(108) Espinosa, E.; Alkorta, I.; Elguero, J.; Molins, E. From weak to strong interactions: a comprehensive analysis of the topological and energetic properties of the electron density distribution involving X–H⋯ F–Y systems. *The Journal of chemical physics* **2002**, *117*, 5529-5542.
(109) Lankau, T.; Yu, C. H. Computational Evidence for Homonuclear $Ge^{I}Ge^{I}$ Dative Bonds. *The Journal of Physical Chemistry A* **2020**, *124*, 3795-3804.
(110) Kasai, H.; Tolborg, K.; Sist, M.; Zhang, J.; Hathwar, V. R.; Filsø, M. Ø.; Cenedese, S.; Sugimoto, K.; Overgaard, J.; Nishibori, E. X-ray electron density investigation of chemical bonding in van der Waals materials. *Nature materials* **2018**, *17*, 249-252.
(111) Becke, A. D.; Edgecombe, K. E. A simple measure of electron localization in atomic and molecular systems. *The Journal of chemical physics* **1990**, *92*, 5397-5403.
(112) Kohout, M.; Savin, A. Influence of core–valence separation of electron localization function. *Journal of computational chemistry* **1997**, *18*, 1431-1439.
(113) Takumi, M.; Ueda, T.; Koshio, Y.; Nishimura, H.; Nagata, K. Optical properties of Ga_2Se_3 under high pressure. *phys. status solidi (b)* **2001**, *223*, 271-274.
(114) González, J.; Rico, R.; Calderón, E.; Quintero, M.; Morocoima, M. Absorption edge of $MnGa_2Se_4$ single crystals under hydrostatic pressure. *phys. status solidi (b)* **1999**, *211*, 45-49.
(115) Rahnamaye Aliabad, H. A.; Basirat, S.; Ahmad, I. Structural, electronical and thermoelectric properties of $CdGa_2S_4$ compound under high pressures by mBJ approach. *J. Mater. Sci.: Mater. Electron.* **2017**, *28*, 16476-16483.
(116) Ganose, A. M.; Jackson, A. J.; Scanlon, D. O. sumo: Command-line tools for plotting and analysis of periodic* ab initio* calculations. *Journal of Open Source Software* **2018**, *3*, 717.
(117) Hinuma, Y.; Pizzi, G.; Kumagai, Y.; Oba, F.; Tanaka, I. Band structure diagram paths based on crystallography. *Computational Materials Science* **2017**, *128*, 140-184.
(118) Togo, A.; Tanaka, I. Spglib: a software library for crystal symmetry search. *arXiv preprint arXiv:1808.01590* **2018**.
(119) Madelung, O. *Semiconductors: data handbook*. Springer Science & Business Media: 2012.
(120) Lübbers, D.; Leute, V. The crystal structure of β-Ga_2Se_3. *J. Solid State Chem.* **1982**, *43*, 339-345.

FIGURES

Figure 1. (Color online) a) Perspective view of α'-Ga_2S_3. Green, yellow and pink balls represent Ga atoms, S atoms and vacancies, respectively. Ga atoms are four-fold coordinated while S1 and S2 atoms on one hand and S3 atoms on the other hand are three- and two-fold coordinated, respectively. b) Lewis dot diagrams for Ga and S atoms and their nearest bonded neighbour atoms. c) View of the α' phase perpendicular to the *c* axis. The arrangement of the vacancies forms the channels along the *c* axis. d) View of the α' phase perpendicular to the *b* axis. Layers based on GaS_4 tetrahedra parallel to the *a*-*b* plane are stacked along the *c* axis; i.e. coincident with the direction of the channels. When vacancies are included, the strong resemblance of the monoclinic structure of the α' phase with the wurtzite structure can be observed.

Figure 2. (Color online) Selected XRD patterns of α'-Ga_2S_3 at several pressures. Tick marks corresponding to the α' phase, impurity and Cu reflections are added at a few pressures to enlighten the appearance/disappearance of diffraction peaks. Down arrows show the disappearance of several reflections of the α' phase at 16.1 GPa.

Figure 3. (Color online) a) Experimental (black solid circles) and theoretical GGA-PBEsol (black solid line) pressure dependence of the unit-cell volume of α'-Ga_2S_3. Experimental Run-2 (blue empty circles) and theoretical LDA (black dash line) from **Ref. 38** are also plotted for comparison. Both experimental data are fit to a BM3-EoS (dotted lines). b) Pressure dependence of the lattice parameters *a*, *b* and *c* of α'-Ga_2S_3. The inset shows the pressure dependence of the monoclinic β angle.

Figure 4. (Color online) a) View of α'-Ga_2S_3 perpendicular to *c* axis where ev_2 is located along *b* axis, covering the major section of the vacancy channels. ev_2 refers to the intermediate direction of compression. b) View of α'-Ga_2S_3 perpendicular to *b* axis, parallel to *a*-*c* plane. ev_1 intersects the small cross-section of the vacancy channels, meanwhile ev_3 is almost normal to the GaS_4-based layers. ev_1 and ev_3 refer to the maximum and the minimum direction of compression, respectively. Ga and S atoms and vacancies are shown in green, yellow and pink, respectively.

Figure 5. (Color online) Pressure dependence of Ga-S bond lengths and compressibilities in the two GaS_4 polyhedra: a) and c) for $Ga1S_4$ and b) and d) for $Ga2S_4$ polyhedra. Ga1-S1* and Ga2-S2* refer the longest bond lengths between the Ga1-S1 and Ga2-S2 atoms, respectively.

Figure 6. (Color online) RS spectra of α'-Ga_2S_3 at selected pressures. The different *A'* and *A''* modes have been tentatively identified in the RS spectra.

Figure 7. (Color online) Pressure dependence of the theoretical (solid lines) and experimental (symbols) Raman-active mode frequencies of α'-Ga_2S_3.

Figure 8. (Color online) RS spectra of α'-Ga_2S_3 at selected temperatures. Up arrows show the appeareance of new peaks at 948 K.

Figure 9. (Color online) Correlation between the temperature and pressure derivatives of the experimental Raman-active mode frequencies. Dashed lines are labelled by the corresponding implicit fraction.

Figure 10. (Color online) Pressure dependence of the charge density $\left(\rho(r)\right)$ and its laplacian $\left(\nabla^2\rho(r)\right)$ for the BCPs.

Figure 11. (Color online) Pressure dependence of the a) H_b/ρ_b, b) G_b/ρ_b and c) $|V_b|/G_b$ ratios for the BCPs.

Figure 12. (Color online) a) View of α'-Ga_2S_3 perpendicular to the *c* axis with the single and double LEPs along the channels at 0 GPa. b) Detail of the single and double LEP volume of the S1 and S3 atoms, respectively, at selected pressures (ELF isosurfaces at $\eta = 0.87$).

Figure 13. (Color online) Pressure dependence of the LEP-S3-LEP and Ga1-S3-Ga2 angles.

Figure 14. (Color online) Electronic band structure and PDOS of α'-Ga_2S_3 at 0 GPa. Red and green points mark the position of the conduction band minimum and valence band maximum, respectively. The 1st valence band (VB) and the 1st and 2nd conduction bands (CB) are labelled.

Figure 15. (Color online) a) Pressure dependence of the theoretical direct and indirect band gaps in α'-Ga_2S_3. b) Pressure dependence of the calculated energies of the three lowest conduction band (CB) minima and valence band (VB) maximum at the Γ point, together with the CB minimum at the V_2' point. Blue solid (dash) line indicate the pressure for the the direct-to-indirect band gap crossover (conduction band anticrossing of the direct band gap) at 5.5. (7.5) GPa.

Figure 1

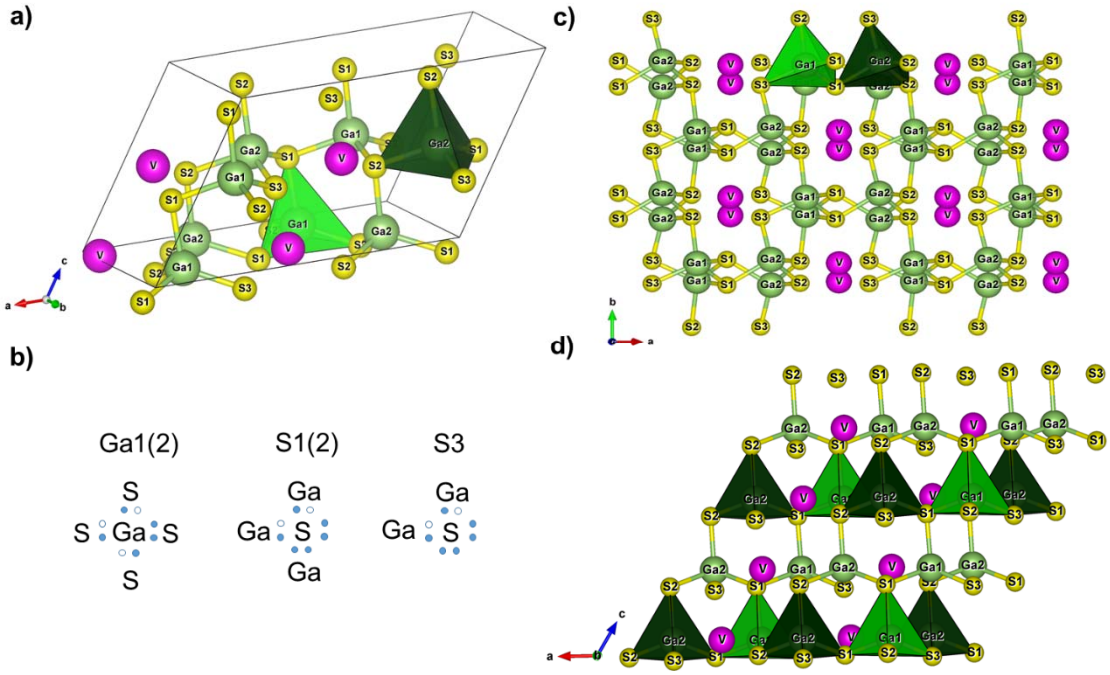

Figure 2

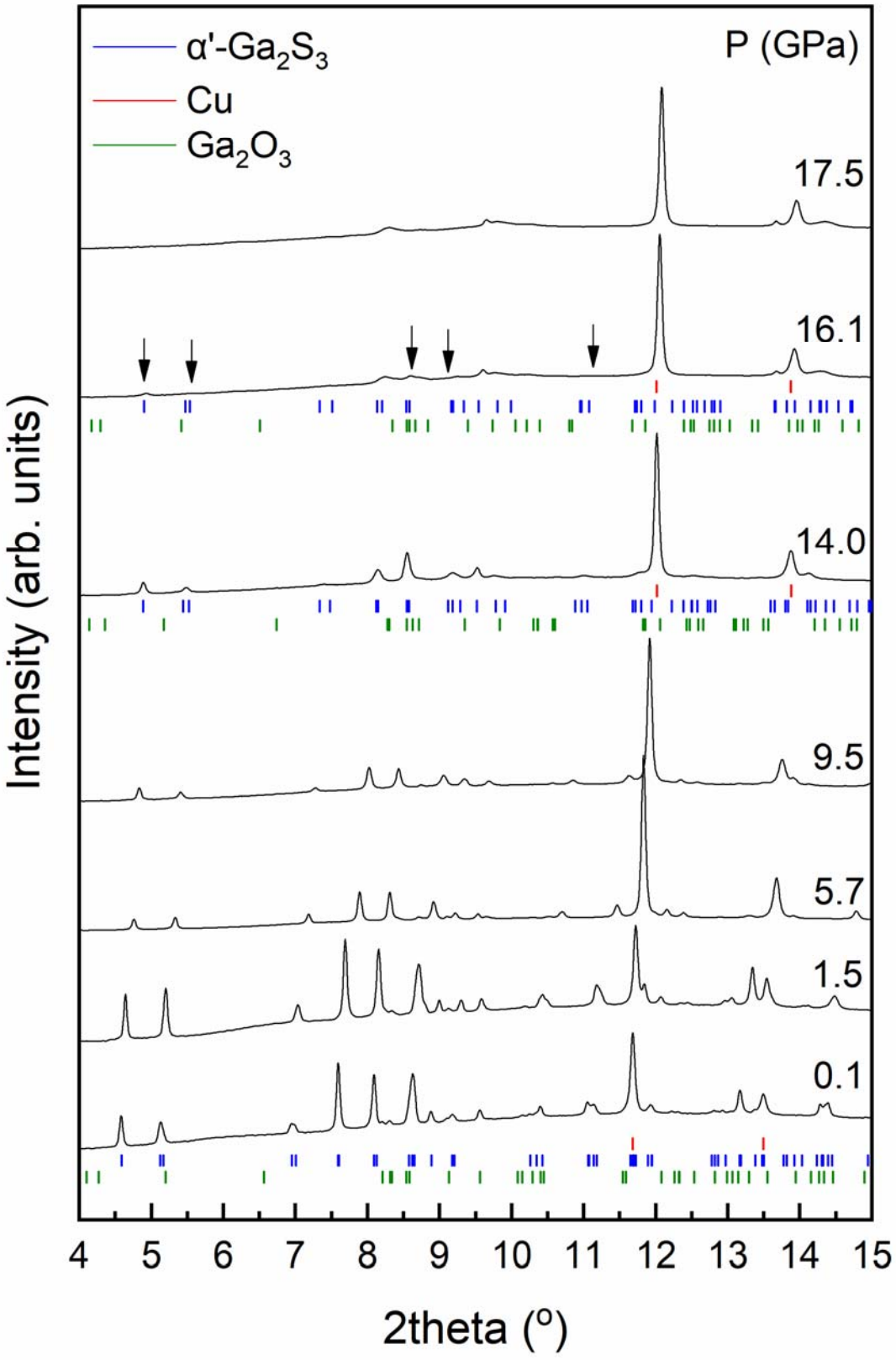
α'-Ga2S3
Cu
Ga2O3
P (GPa)
17.5
16.1
14.0
9.5
5.7
1.5
0.1
Intensity (arb. units)
4
5
6
7
8
9
10
11
12
13
14
15
2theta (°)

Figure 3

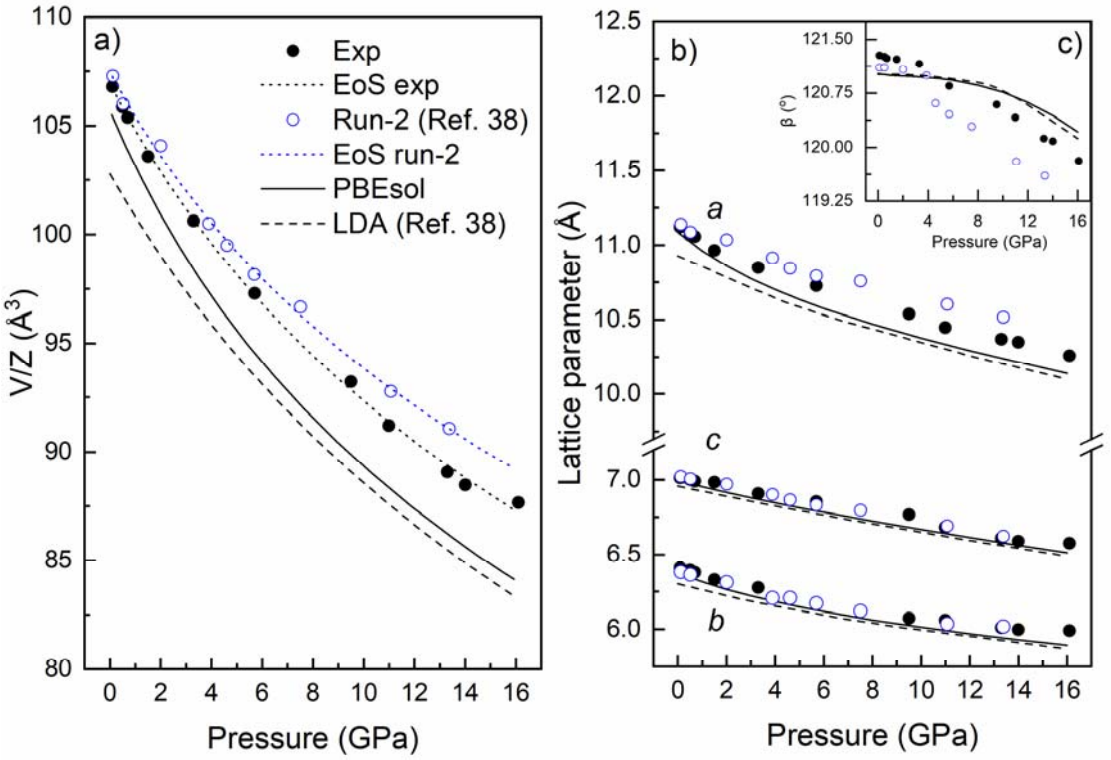
a)
Exp
EoS exp
Run-2 (Ref. 38)
EoS run-2
PBEsol
LDA (Ref. 38)
V/Z (Å^3)
Pressure (GPa)
b)
c)
a
c
b
Lattice parameter (Å)
β (°)
Pressure (GPa)

Figure 4

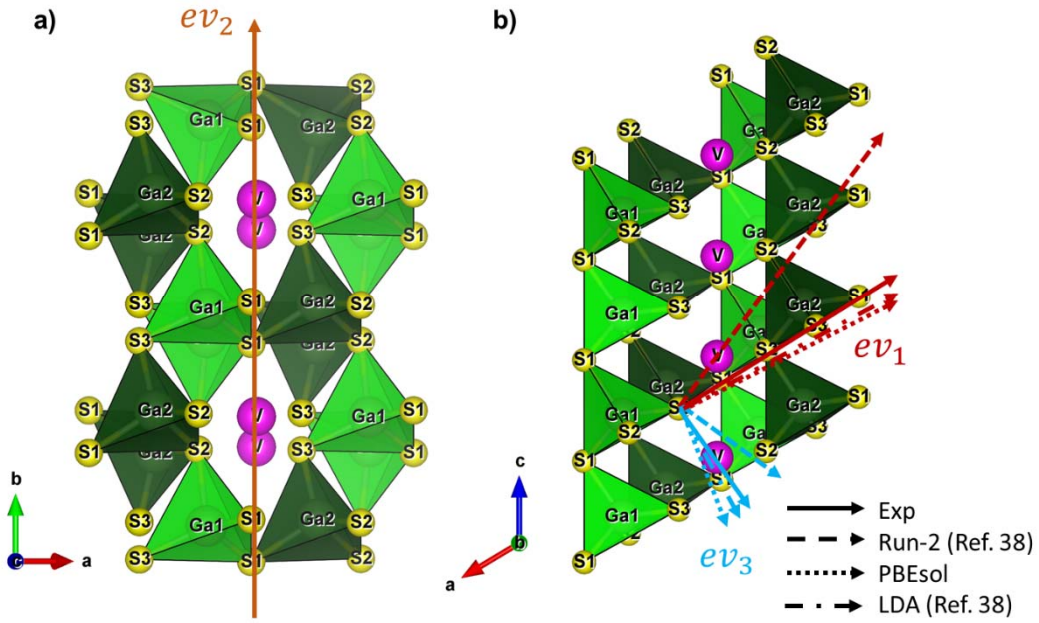

Figure 5

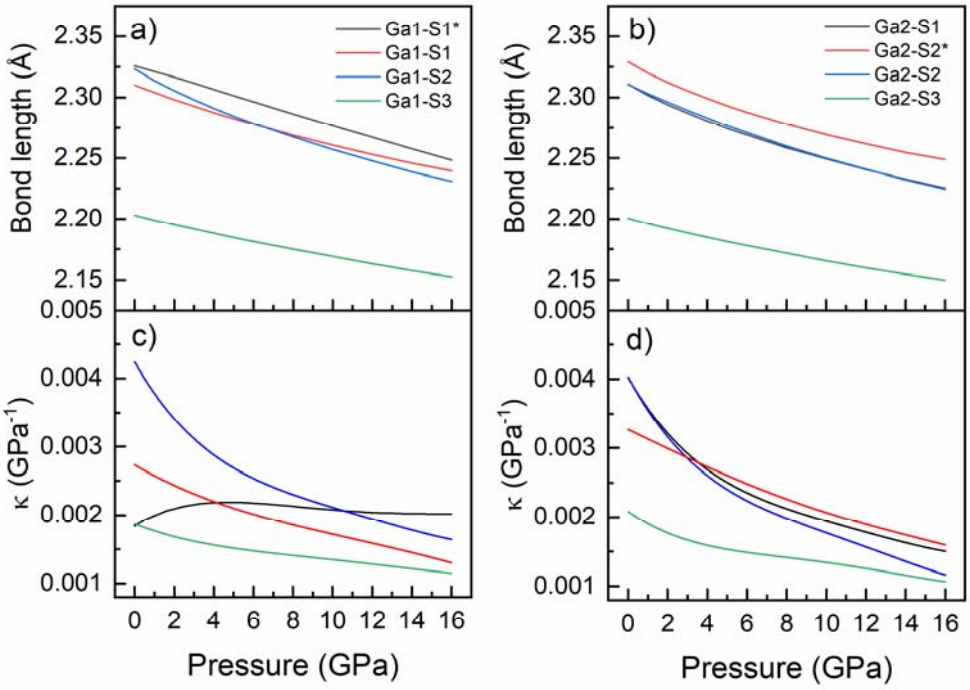
a)
b)
c)
d)
Ga1-S1*
Ga1-S1
Ga1-S2
Ga1-S3
Ga2-S1
Ga2-S2*
Ga2-S2
Ga2-S3
Bond length (Å)
κ (GPa-1)
Pressure (GPa)
2.35
2.30
2.25
2.20
2.15
0.005
0.004
0.003
0.002
0.001
0 2 4 6 8 10 12 14 16

Figure 6

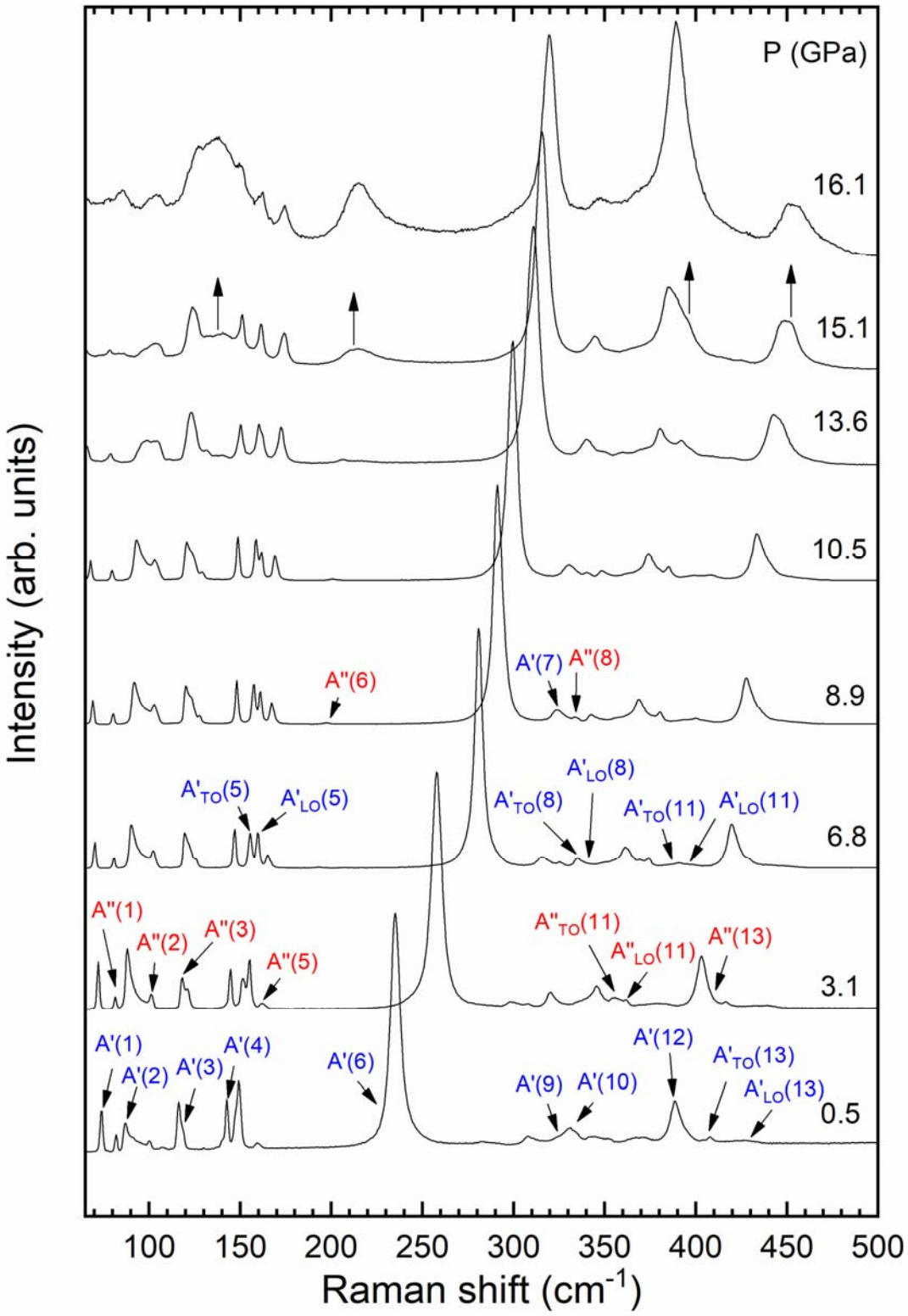
P (GPa)
16.1
15.1
13.6
10.5
8.9
6.8
3.1
0.5
A''(6)
A'(7)
A''(8)
A'TO(5)
A'LO(5)
A'TO(8)
A'LO(8)
A'TO(11)
A'LO(11)
A''(1)
A''(2)
A''(3)
A''(5)
A''TO(11)
A''LO(11)
A''(13)
A'(1)
A'(2)
A'(3)
A'(4)
A'(6)
A'(9)
A'(10)
A'(12)
A'TO(13)
A'LO(13)
Intensity (arb. units)
100
150
200
250
300
350
400
450
500
Raman shift (cm-1)

Figure 7

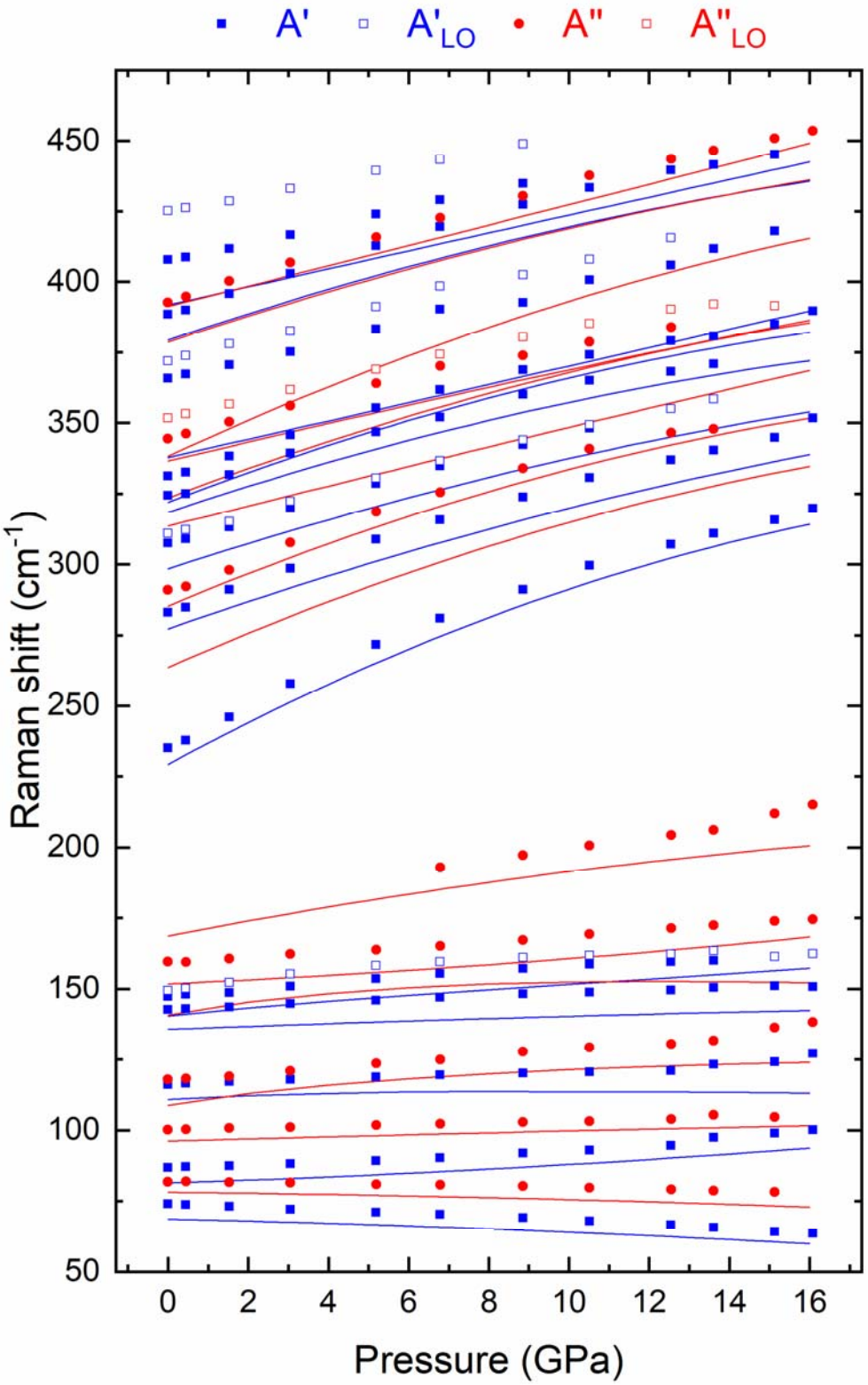
A'
A'LO
A"
A"LO
Raman shift (cm-1)
Pressure (GPa)
50
100
150
200
250
300
350
400
450
0
2
4
6
8
10
12
14
16

Figure 8

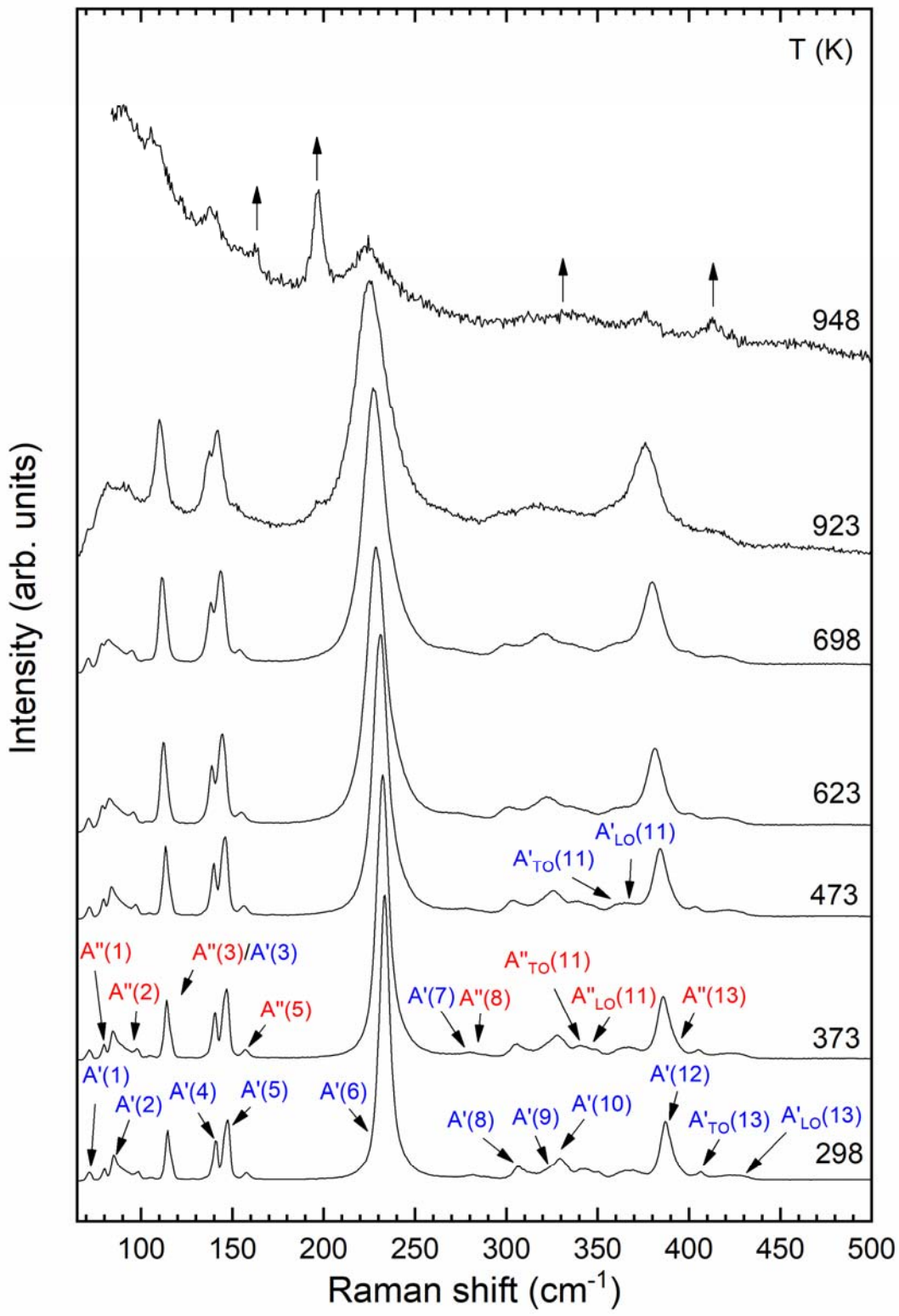
T (K)
948
923
698
623
473
373
298
Intensity (arb. units)
Raman shift (cm-1)
100
150
200
250
300
350
400
450
500
A"(1)
A"(2)
A"(3)/A'(3)
A"(5)
A'(7)
A"(8)
A"TO(11)
A"LO(11)
A"(13)
A'TO(11)
A'LO(11)
A'(1)
A'(2)
A'(4)
A'(5)
A'(6)
A'(8)
A'(9)
A'(10)
A'(12)
A'TO(13)
A'LO(13)

Figure 9

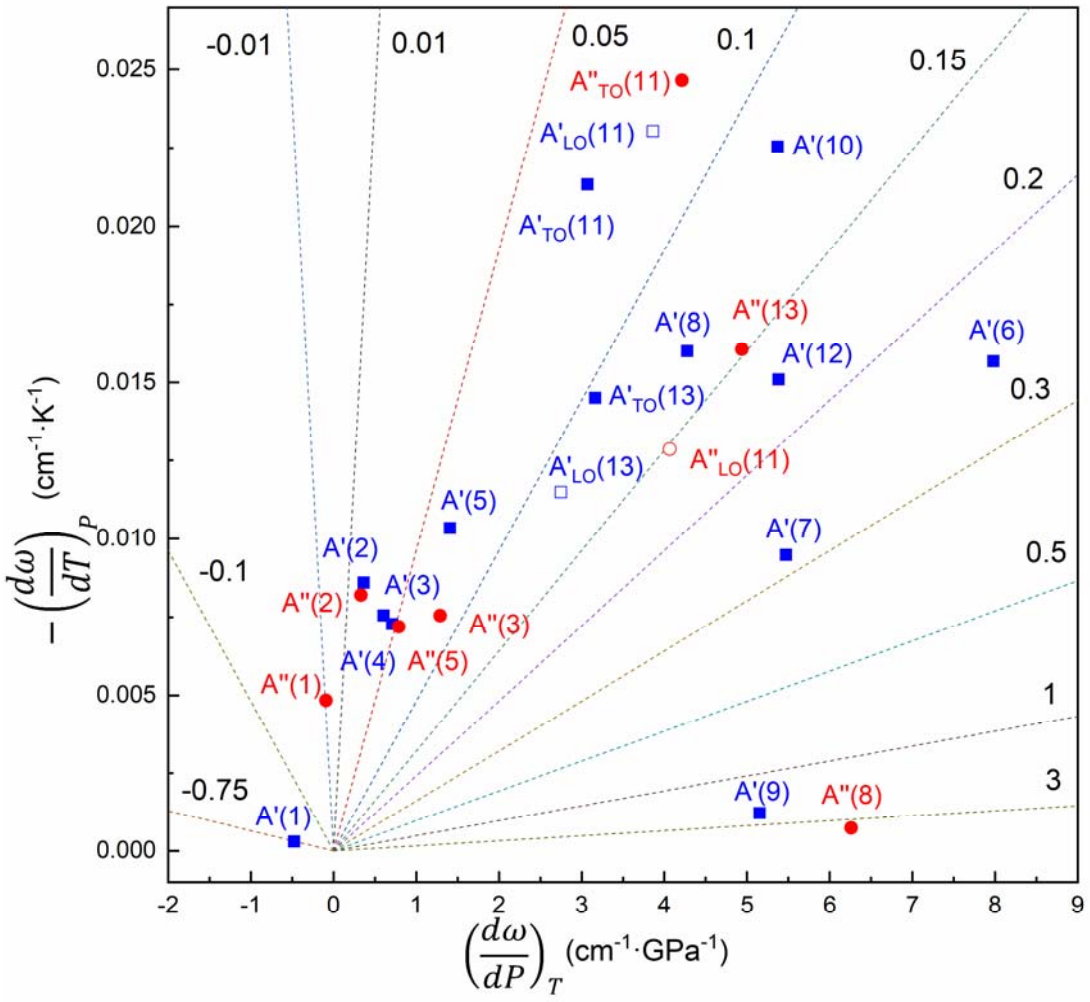
-0.01
0.01
0.05
0.1
0.15
0.2
0.3
0.5
1
3
-0.1
-0.75
A"TO(11)
A'LO(11)
A'(10)
A'TO(11)
A'(8)
A"(13)
A'(6)
A'(12)
A'TO(13)
A'LO(13)
A"LO(11)
A'(5)
A'(7)
A'(2)
A'(3)
A"(2)
A"(3)
A'(4)
A"(5)
A"(1)
A'(1)
A'(9)
A"(8)
0.025
0.020
0.015
0.010
0.005
0.000
-2
-1
0
1
2
3
4
5
6
7
8
9
$-\left(\frac{d\omega}{dT}\right)_P$ (cm^{-1}·K^{-1})
$\left(\frac{d\omega}{dP}\right)_T$ (cm^{-1}·GPa^{-1})

1329 **Figure 10**

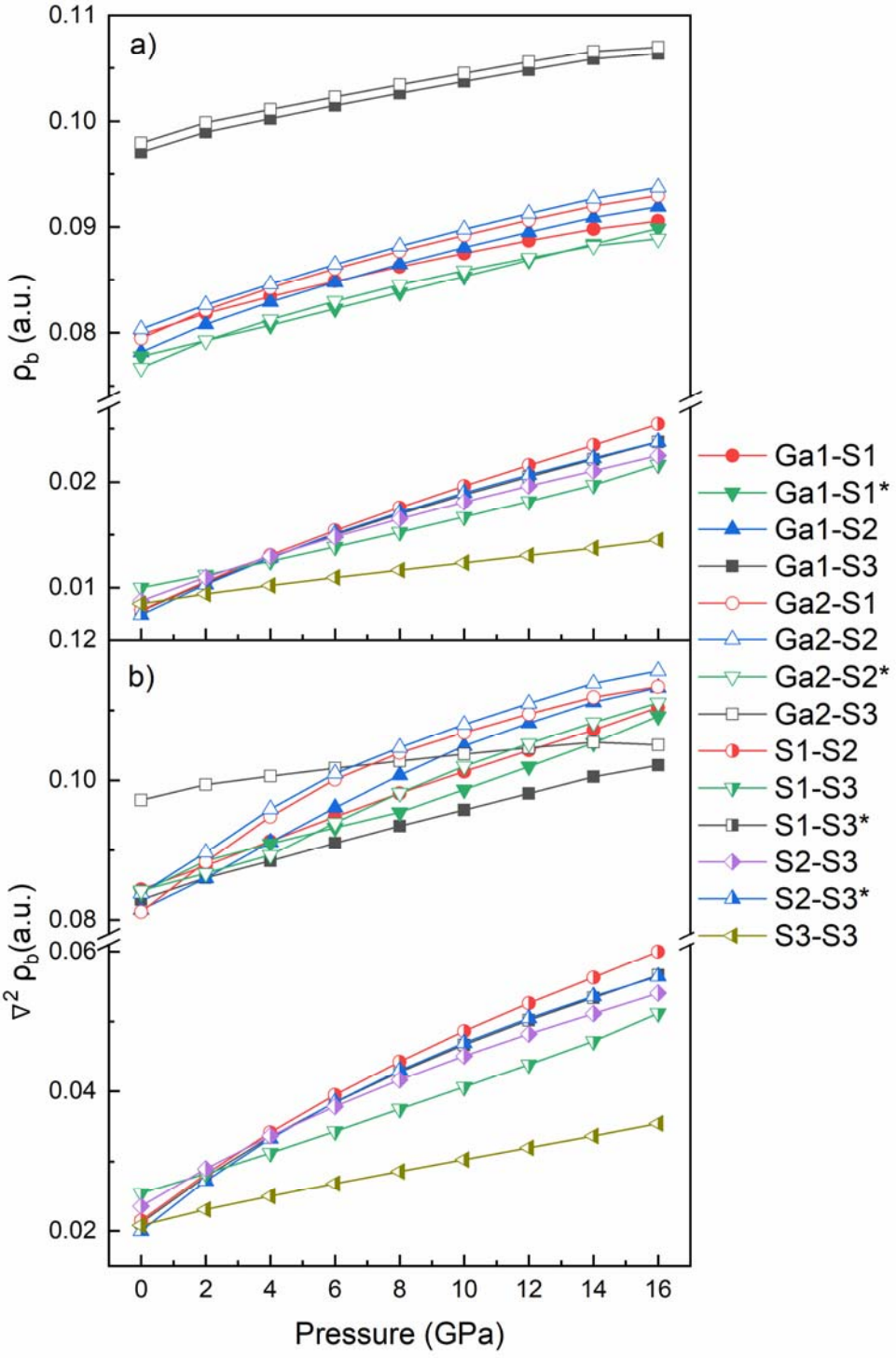

1330

Figure 11

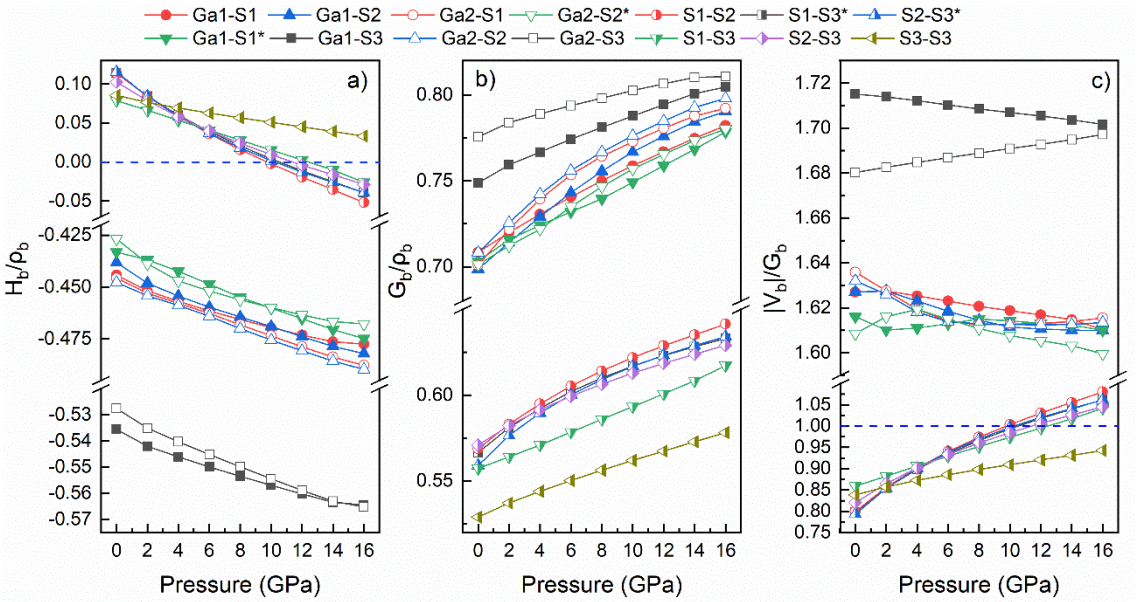
Ga1-S1
Ga1-S2
Ga2-S1
Ga2-S2*
S1-S2
S1-S3*
S2-S3*
Ga1-S1*
Ga1-S3
Ga2-S2
Ga2-S3
S1-S3
S2-S3
S3-S3
a)
b)
c)
H_b/ρ_b
G_b/ρ_b
$|V_b|/G_b$
Pressure (GPa)
Pressure (GPa)
Pressure (GPa)

Figure 12

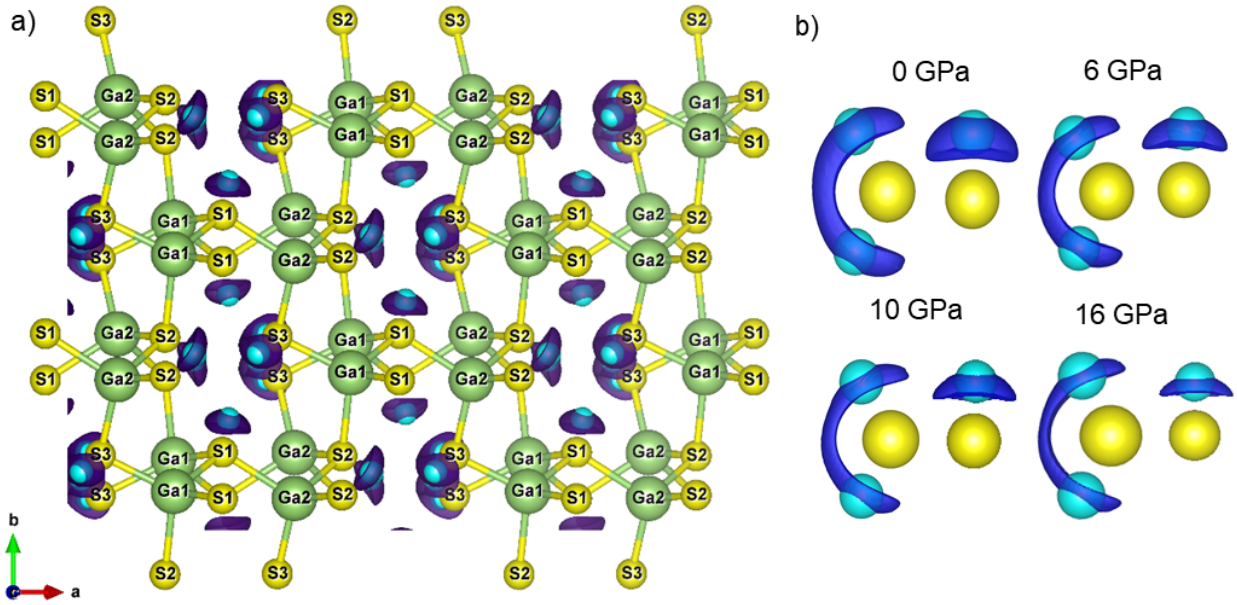

Figure 13

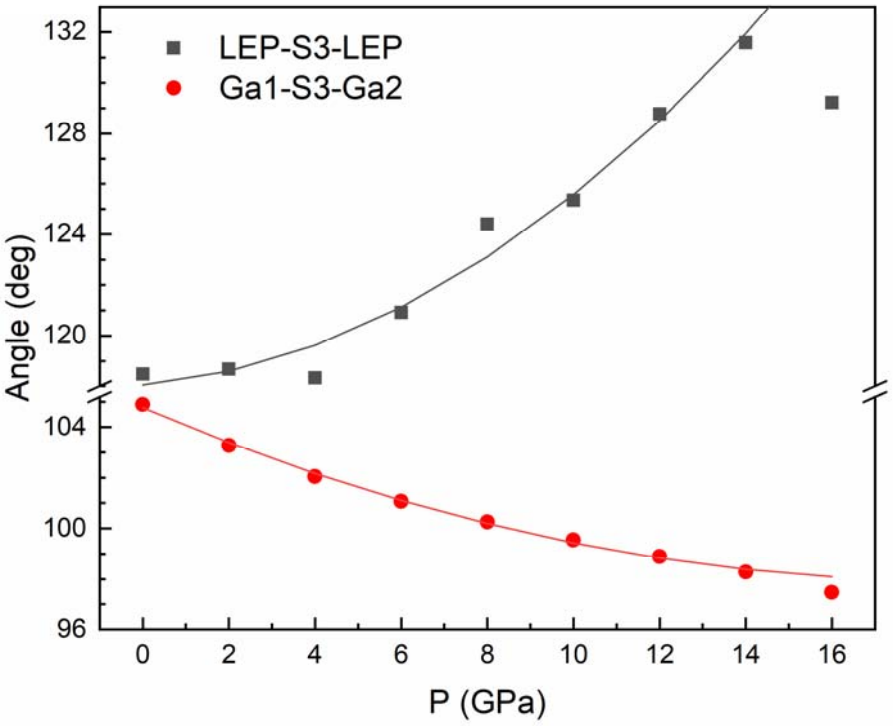
LEP-S3-LEP
Ga1-S3-Ga2
Angle (deg)
P (GPa)
132
128
124
120
104
100
96
0
2
4
6
8
10
12
14
16

Figure 14

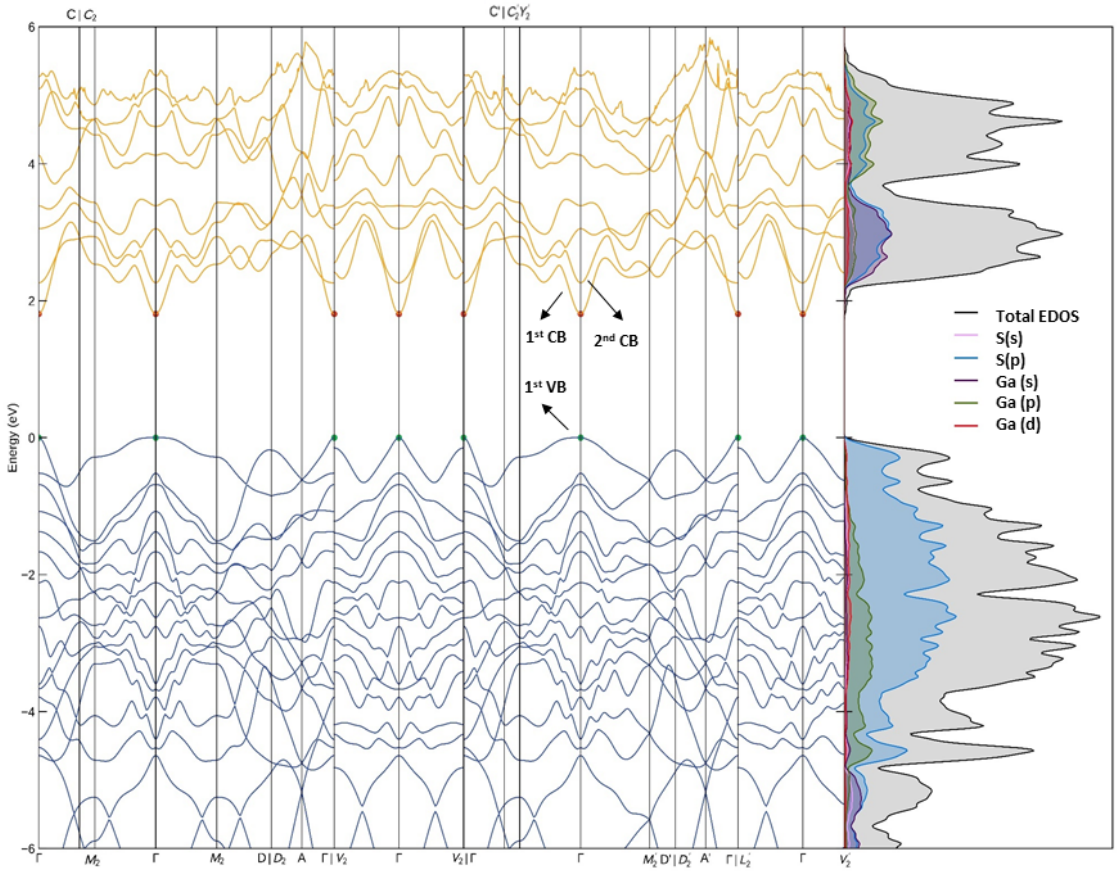
C | C2
C' | C2'Y2'
6
4
2
0
−2
−4
−6
Energy (eV)
1st CB
2nd CB
1st VB
Total EDOS
S(s)
S(p)
Ga (s)
Ga (p)
Ga (d)
Γ
M2
Γ
M2
D | D2
A
Γ | V2
Γ
V2 | Γ
Γ
M2 D' | D2'
A'
Γ | L2'
Γ
V2'

1344 **Figure 15**

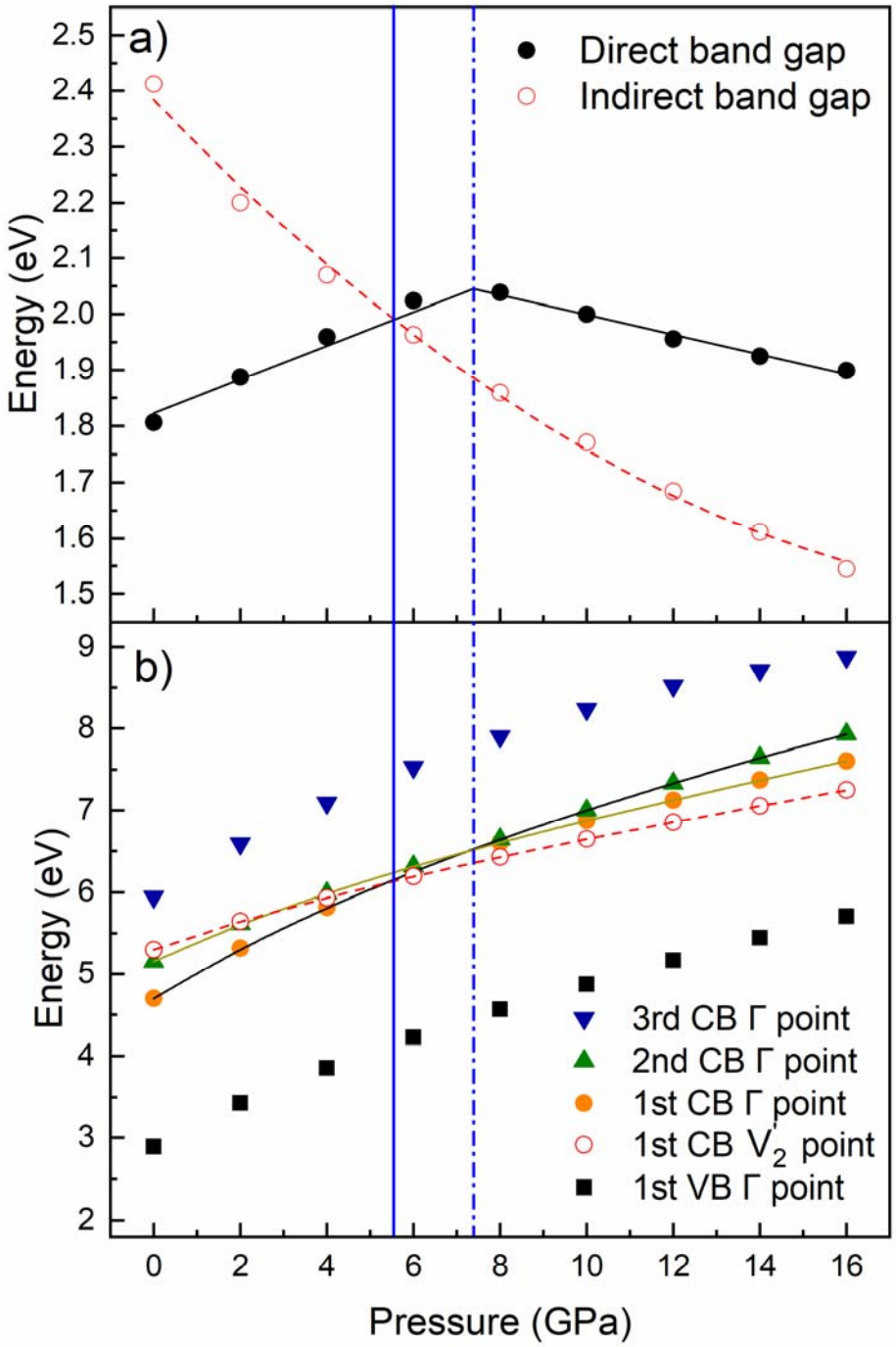

1345

Table 1. Zero-pressure volume (V_o), bulk modulus (B_o) and pressure derivative (B_o') from BM3-EoS. Our experimental (Exp) and theoretical (GGA-PBEsol) values are compared to experimental (Run-2) and theoretical (LDA) data from **Ref. 38**. The same parameters are shown for the isostructural β-Ga_2Se_3.

	α'-Ga_2S_3				β-Ga_2Se_3	
	Exp	Run-2[38]	GGA-PBEsol	LDA[38]	Exp	GGA-PBE[74]
V_o (Å^3)	427.8 (3)	429 (2)	423.1 (3)	411.1 (3)	488.4[120]	467.5
B_o(GPa)	47 (5)	49 (5)	38.0 (6)	49.6 (8)	51[73]	39.9
B_o'	5 (1)	6 (1)	5.3 (1)	4.1 (2)		4.7

Table 2. Axial compressibilities, principal axes (ev_i) and their compressibillities (λ_i), and angles of maximum (ψ_{max}) and minimum compression (ψ_{min}) in α'-Ga_2S_3 from 0 to 14 GPa. Our experimental (Exp) and theoretical (GGA-PBEsol) data are compared to experimental (Run-2) and theoretical (LDA) data from **Ref. 38**. ψ_{max} and ψ_{min} are measured to the *c* axis (from c to a).

	Exp	Run-2[38]	GGA-PBEsol	LDA[38]
κ_a (10^{-3} GPa)	9.05	6.36	10.98	7.49
κ_b (10^{-3} GPa)	12.76	8.86	9.62	6.85
κ_c (10^{-3} GPa)	4.317	4.93	5.39	4.82
λ_1 (TPa^{-1})	5.53	4.81	5.04	5.02
ev_1	(-0.963, 0, -0.270)	(-0.833, 0, 0.553)	(-0.940,0, -0.341)	(-0.958, 0, -0.286)
λ_2 (TPa^{-1})	5.05	4.57	4.52	4.35
ev_2	(0, 1, 0)	(0, 1, 0)	(0, 1, 0)	(0, 1, 0)
λ_3 (TPa^{-1})	3.29	2.52	3.88	3.68
ev_3	(-0.231, 0, -0.973)	(-0.436, 0, -0.900)	(-0.201, 0, -0.980)	(-0.224, 0, -0.975)
ψ_{max} (°)	68.6	43.0	71.7	69.4
ψ_{min} (°)	158.2	132.5	164.6	159.2